Nonlinear Rheology of Entangled Wormlike Micellar Solutions Predicted by A Micelle-Slip-Spring Model

Takeshi Sato¹ and Ronald G. Larson^{2, a)}

¹⁾Institute for Chemical Research, Kyoto University, Uji 611-0011,

Japan

²⁾Department of Chemical Engineering, University of Michigan, Ann Arbor, MI 48109,

USA

(Dated: 1 March 2022)

We examine linear and nonlinear shear and extensional rheological properties using a "micelle slip-spring model" [T. Sato et al., J. Rheol., 64, 1045 (2020)] that incorporates breakage and rejoining events into the slip-spring model originally developed by Likhtman for unbreakable polymers [Macromolecules, 38, 6128 (2005)]. We here employ the Fraenkel potential for main chain springs and slip-springs to address the effect of the finite extensibility. Moreover, to improve extensional properties under strong extensional flow, stress-induced micelle breakage (SIMB) is incorporated into the micelle slip-spring model. Thus, this model is the first model that includes the entanglement constraint, Rouse modes, finite extensibility, breakage and rejoining events, and stress-induced micelle breakage. Computational expense currently limits the model to micellar solutions with moderate numbers of entanglements (≤ 7), but for such solutions nearly quantitative agreement is attained for start-up of shearing flow. The model in extensional flow cannot yet be tested owing to the lack of data for this entanglement level. The transient and steady shear properties predicted by the micelle slip-spring model for a moderate shear rate region without significant chain stretch are fit well by the Giesekus model but not by the Phan/Thien-Tanner (PTT) model, which is consistent with the ability of the Giesekus model to match experimental shear data. The extensional viscosities obtained by the micelle slip-spring model with SIMB show thickening followed by thinning, which is in qualitative agreement with experimental trends. Additionally, the extensional rheological properties of the micelle slip-spring model with or without SIMB are poorly predicted by both the Giesekus and the PTT models using a single nonlinear parameter. Thus, future work should seek a constitutive model able to capture the behavior of the slip-spring model in shear and extensional flows, and so provide an accurate, efficient model of micellar solution rheology.

a) Electronic mail: rlarson@umich.edu

I. INTRODUCTION

Surfactant molecules, consisting of a hydrophilic head and hydrophobic tail, are widely utilized in our daily life. They form self-assembled structures, such as spherical and cylindrical micelles, depending on surfactant and salt compositions. Cylindrical micelles or wormlike micelles (WLMs) with entanglements typically show significant viscoelastic properties, and have attracted significant attention from the rheological community.

There have been extensive experimental studies that examine linear rheology,^{2–4} nonlinear shear rheology, 5-12 nonlinear extensional rheology, 13-17 as well as the corresponding microstructures of WLMs. 18-20 In this study, we especially focus on modeling the nonlinear rheological properties of WLM solutions, and begin by briefly summarizing the relevant experimental studies. If the WLM solutions remain spatially homogeneous, their rheological properties are similar to those of entangled polymers; that is, the transient shear viscosity growth shows a stress overshoot, and the steady shear viscosity shows shear thinning.^{5–7} An important finding is that the Giesekus model, which is a common phenomenological constitutive equation,²¹ can accurately reproduce the shear rheological properties of WLM solutions.^{8,9} An important difference in shear rheological properties between WLM and polymer solutions can be observed however at high shear rates, where macroscopic flows can become spatially inhomogeneous. An example of this is shearbanding^{22,23} which has been extensively investigated for example by Helgeson and coworkers for cetyltrimethylammonium bromide (CTAB) solutions modeled using the Giesekus equation with a stress-diffusion term. 10,11 Extensional flow properties of WLM solutions can be measured by several experimental techniques, ²⁴ such as filament-stretching extensional rheometry (FiSER), ¹³ capillary breakup extensional rheometry (CaBER),¹⁴ and the opposed jet device.^{15–17} Rothstein and coworkers reported that the WLM solutions show strain hardening followed by the filament rupture before reaching a steady state. This filament rupture was considered to be due to flowinduced scission of micelle chains. Steady extensional viscosities measured by the opposed jet device for several surfactant and salt systems show extension thickening followed by extension thinning. 15–17

To deeply understand such experimental findings, theoretical and numerical approaches are highly desirable. From a theoretical perspective, Cates developed a so-called reptation-reaction model to describe linear "living" polymers²⁵ that can break at a random point along a chain and whose ends can each randomly fuse with the end of some other chain in a reversible scis-

sion scheme. The reptation-reaction model can successfully capture the Maxwell-type relaxation with a single relaxation time as observed in experiments.² However, other polymer-like relaxation mechanisms, including chain-length fluctuations and constraint release, which are important to reproduce the rheology of entangled polymers, are not addressed in the original Cates' model. (In addition to reversible scission, Turner and Cates considered an end-interchange scheme that makes a three-arm star intermediate, and a bond-interchange scheme that makes a four-arm star intermediate.²⁶ They showed that the relaxation behavior is changed by these mechanisms.)

Based on Cates' reaction-reptation model, the "pointer algorithm" was developed by Zou and Larson to accurately predict the linear rheology of WLM solutions.²⁷ In the pointer algorithm, reptation, chain length fluctuations, and constraint release are combined with breakage/rejoining. To compute the relaxation modulus, the boundaries between relaxed and unrelaxed parts of WLM chains are tracked. Analytic formulas for the high-frequency modes are then added to account for the high-frequency region. Zou and Larson showed this pointer algorithm can reproduce linear rheological properties over a wide frequency range.²⁷ After their original work, the pointer algorithm was extended in several directions; e.g., the end-interchange and bond-interchange schemes were addressed,²⁸ and relaxation mechanisms of unentangled micelles were included.²⁹ More recently, Tan and coworkers have established a formula based on the pointer algorithm simulations to estimate micelle length from linear rheological data.³⁰ Utilizing the pointer algorithm, we can thus obtain accurate microscopic micelle parameters from linear rheological data. Compared to these modeling developments in linear rheology, nonlinear rheological models are relatively underdeveloped.

One of the most utilized models for the nonlinear rheology of WLMs is the Vasquez-Cook-McKinley (VCM) model.³¹ The VCM model is composed of two species of Hookean dumbbells: long and short dumbbells. A long dumbbell can break to make two short dumbbells and vice versa to mimic the reversible scission scheme. Since the Hookean dumbbell model is employed, the VCM model with a constant breakage rate cannot reproduce nonlinear rheological properties, such as shear thinning observed in WLM solutions. Thus, the VCM model includes the stress-induced micelle breakage under flow.³¹ While several nonlinear properties under homogeneous flow have been successfully reproduced by the VCM model,³² the effects of entanglements (i.e., the constraints they imposed on chain relaxation, and how they might be lost and gained under flow) are not included in the VCM model, which thus neglects the most important source of shear thinning in WLM solutions. Shear thinning is predicted by the VCM model, but only through

inclusion of shear-induced micelle breakage, whose rate is adjusted arbitrarily to produce shear thinning strong enough to agree with experiments.

Very recently, Peterson and coworkers developed two molecular-based constitutive models for entangled WLM solutions.^{33–35} One is the simplified tube approximation for rapid-breaking micelles (STARM) model,³³ and the other model is the living Rolie-Poly model.³⁴ The basic idea of these models is to combine the population balances and polymeric relaxations, i.e., reptation, contour length fluctuation, and constraint release. While these models are physics-based and sophisticated, it is difficult to implement them in macroscopic flow calculations due to their model complexity. It should be noted that there is a simplified version of the living Rolie-Poly model in the fast-breakage limit, where micelle breakage is much faster than reptation, that might be used for macroscopic flow calculations. However, the fast-breakage limit is often not attained in common micellar solutions and, to the best of our knowledge, a simplified physics-based constitutive model beyond the fast-breakage limit has not been developed yet. To avoid the complexity appearing in these constitutive models, it may be useful instead to develop an accurate mesoscopic simulation model and fit the predictions of this model with a simpler constitutive equation. This strategy would allow a tractable equation to be developed whose parameters could be correlated with micelle properties, rather than simply being adjusted to fit the experiments, without yielding any connection to microscopic physics.

We developed such a mesoscopic "micelle slip-spring simulation model" to predict rheological properties of WLM solutions.³⁶ Our model is based on the slip-spring model originally proposed by Likhtman.³⁷ Slip-link and slip-spring models were originally developed for unbreakable entangled polymers, and have been found to predict well their linear and nonlinear rheological properties.³⁸ To address the rheology of WLM solutions, breakage and rejoining events were included in the polymer slip-spring model and the results were validated through comparison with predictions of the pointer algorithm and with experimental linear viscoelastic data. Moreover, using the micelle slip-spring model, we examined nonlinear shear properties including shear thinning, which naturally emerge from our micelle slip-spring model due to the effect of the entanglement constraint.³⁶

In this paper, we further investigate nonlinear rheological properties obtained by the micelle slip-spring model. For such a purpose, instead of the Hookean springs utilized in our previous study following the original slip-spring model,³⁶ we use the Fraenkel springs to prevent the overstretch of springs so that higher shear rates and extensional flows can be simulated where finite

extensibility of the chain becomes important. Additionally, to improve extensional properties under strong extensional flow, we incorporate stress-induced micelle breakage into the micelle slip-spring model. Using the extended micelle slip-spring model, we examine nonlinear shear and extensional properties. Details are explained in the following sections.

II. MODEL

A. Original Micelle-slip-spring Model

Here, we briefly explain the original micelle slip-spring model. ³⁶ A micellar chain is expressed by a main chain and slip-springs that impose motional constraints on the main chain, as shown in the upper figure in Fig. 1. A micellar chain i ($1 \ge i \ge N_{\text{chain}}(t)$) consists of $N^{(i)}(t) + 1$ beads connected by $N^{(i)}(t)$ springs. Here, the super-script (i) distinguishes different micellar chains, and $N_{\text{chain}}(t)$ is the number of micellar chains in the system at time t. Because of breakage and rejoining events, $N_{\text{chain}}(t)$ and $N^{(i)}(t)$ fluctuate in time in our micelle slip-spring model.

Each main chain spring is modeled by a single Kuhn segment with Kuhn length b, and each main chain bead is given a friction coefficient ξ . Here, the Kuhn length is related to the persistence length ℓ_p as $b=2\ell_p$. ³⁹ On length scales is less than ℓ_p , the chain is locally rigid.

The main chain i has $Z_{ss}^{(i)}(t)$ slip-springs at time t. A slip-spring illustrated in Fig. 1 consists of a slip-link shown with the red open circle connected to an anchoring point shown with the red filled diamond by a red slip-spring. The slip-link k on the chain i, $s_k^{(i)}$, is constrained to move along the

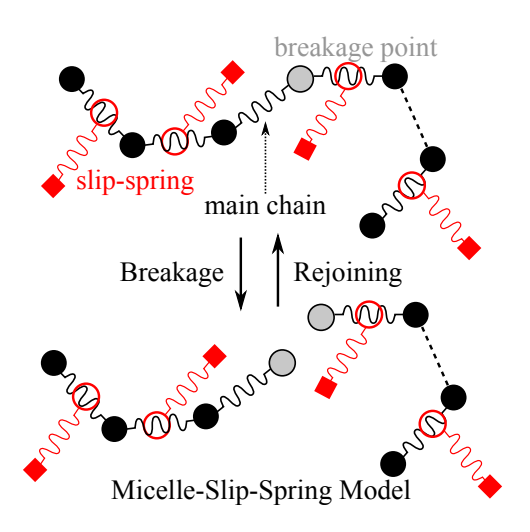


FIG. 1. Schematic illustration of the micelle-slip-spring model.

main chain *i*. Different from current "discrete" slip-spring models, in which the positions of the slip-links are restricted to jump main chain beads, 40,41 in our model, as in the original slip-spring model of Likhtman, the slip-links can move anywhere along the chain. The time evolution of $s_k^{(i)}$ is defined by a 1D continuous dummy variable $x_k^{(i)}$, which spans between 0 and $N^{(i)}(t)$. In this study, slip-links are allowed to pass through each other since this has little effect on the results, as noted by Likhtman. While the slip-link can travel along the main chain, the corresponding anchoring point, $a_k^{(i)}$, is pinned in space unless flow is applied. When shear or extensional flow is applied, the anchoring point moves affinely, as in our previous study.

Each slip-spring has N_s Kuhn segments with the Kuhn length b_{ss} , and each slip-link has a friction coefficient ξ_s . As in our previous study³⁶ that follows the original study by Likhtman,³⁷ we assume that the Kuhn length of main chain springs is the same as that of slip-springs (i.e., $b = b_{ss}$). The slip-link friction coefficient ξ_s is introduced to control the dynamics of the slip-springs. The initial number of slip-springs per chain is determined by an additional parameter, the average number of beads between slip-links, N_e^{ss} . The slip-links are initially distributed randomly along the chains, and the anchoring points are placed around the corresponding slip-links according to a Gaussian potential of a Hookean spring as in the original model of Likhtman³⁷ even though we employ the Fraenkel potential. We note that the microscopic detail of the model should not appear in long-time rheological behavior, and thus the effect of this approximation would be expected to vanish in the long-time region.

The remaining relaxation mechanism needed to reproduce the dynamics of entangled polymers is constraint release (CR). We implement CR as in the original Likhtman's slip-spring model, ³⁷ in which a slip-link is paired with a partner slip-link on a different chain. The CR occurs when the slip-link slides off the end of the chain (i.e., $x_k^{(i)}(t) < 0$ or $N^{(i)}(t) < x_k^{(i)}(t)$). When CR occurs, this slip-link and the partner slip-link are removed from the chain and the partner chain, respectively. At the same time, two new slip-links are placed on two different randomly chosen chains. One slip-link is placed near the end of a chain, and the other is placed at a random position on a different chain. The corresponding anchoring points are distributed using the same procedure explained previously. Thus, while the number of slip-springs on a given chain i, $Z_{\rm ss}^{(i)}(t)$, fluctuates in time due to CR or breakage/rejoining events, the total number of slip-springs in the system is unchanged even under flow in most of our simulations. However, the effects of flow-induced reduction of entanglement density are quite possibly important, ⁴² and are therefore considered Sec. III D, where we have examined a limiting case in which the total number of entanglements

continuously decreases and eventually becomes zero.

In the original micelle-slip-spring model, we utilized a Hookean spring law following the original polymer slip-spring model. However, in this study, we focus on nonlinear shear and extensional properties of entangled WLMs. Thus, it is important to address the effect of finite extensibility. For springs that each correspond to a single Kuhn length, it is typical to employ the Fraenkel spring law.⁴³ The total potential energy of the chain i is then expressed as

$$U^{(i)} = K \frac{k_{\rm B}T}{2b^2} \sum_{j=1}^{N^{(i)}} \left(R_j^{(i)} \left(b \right)^2 + K_{\rm ss} \frac{k_{\rm B}T}{2N_{\rm s}b_{\rm ss}^2} \sum_{k=1}^{Z_{\rm ss}^{(i)}} \left(q_k^{(i)} \left(\overline{N_{\rm s}}b_{\rm ss} \right)^2 \right),$$
(1)

where K and K_{ss} are the Fraenkel parameters for main-chain springs and slip-springs, respectively, $k_{\rm B}$ is the Boltzmann constant, T is the temperature, $\mathbf{R}_{j}^{(i)}$ is the vector between two adjacent beads defined as $\mathbf{R}_{j}^{(i)} = \mathbf{r}_{j+1}^{(i)}$ $\mathbf{r}_{j}^{(i)}$ with $\mathbf{r}_{j}^{(i)}$ being the position of the j-th bead on the i-th main chain, and $\mathbf{q}_{k}^{(i)}$ is the vector between the slip-link and the anchoring point defined as $\mathbf{q}_{k}^{(i)} = \mathbf{a}_{k}^{(i)}$ $\mathbf{s}_{k}^{(i)}$. Using this potential, we can express the spring force originating from spring j of the main chain, $\mathbf{F}_{\mathrm{sp},j}^{(i)}$, as

$$\boldsymbol{F}_{\mathrm{sp},j}^{(i)} = \frac{\partial U^{(i)}}{\partial \boldsymbol{R}_{j}^{(i)}} = K \frac{k_{\mathrm{B}} T}{b^{2}} \left(R_{j}^{(i)} \left(B_{j}^{(i)} \left(R_{j}^{(i)} \left(R_{j}^{(i)}$$

Furthermore, the spring force originating from slip-spring k, $\boldsymbol{F}_{\mathrm{ss},k}^{(i)}$, can be written as

$$\boldsymbol{F}_{\mathrm{ss},k}^{(i)} = \frac{\partial U^{(i)}}{\partial \boldsymbol{q}_{k}^{(i)}} = K_{\mathrm{ss}} \frac{k_{\mathrm{B}} T}{N_{\mathrm{s}} b_{\mathrm{ss}}^{2}} \left(\boldsymbol{q}_{k}^{(i)} \left(\boldsymbol{\overline{N}_{\mathrm{s}}} b_{\mathrm{ss}} \left(\frac{\boldsymbol{q}_{k}^{(i)}}{\boldsymbol{q}_{k}^{(i)}} \right) \right) \right)$$
(3)

From these forces, bead and slip-link positions are updated over time. For more details regarding the dynamical equations, please see our previous study.³⁶

From the forces and conformations of main chains and slip-springs, the $\alpha\beta$ (α , β / (x, y, z)) components of the stress tensor of the main chain (i.e., real chain) and of the virtual-spring are expressed as

$$\sigma_{\alpha\beta}^{R} = c_{\text{chain}} \left. \sum_{j=1}^{N^{(i)}} F_{\text{sp},j\alpha}^{(i)} R_{j\beta}^{(i)} \right. , \tag{4}$$

$$\sigma_{\alpha\beta}^{V} = c_{\text{chain}} \sum_{k=1}^{Z_{\text{ss}}^{(i)}} F_{\text{ss},k\alpha}^{(i)} q_{k\beta}^{(i)} , \qquad (5)$$

respectively, where c_{chain} is the chain concentration, and $\rangle x = is$ the ensemble average. To compute the relaxation modulus G(t) accurately from an equilibrium simulation using the Green-Kubo formula, Ramírez and coworkers pointed out that the virtual-spring stress tensor $\sigma_{\alpha\beta}^{V}$ needs to be included so that

$$G(t) = \frac{\sigma_{xy}^{R}(t)}{\gamma}$$

$$= \frac{V}{k_{B}T} \left\{ \left\langle \sigma_{xy}^{R}(t) \sigma_{xy}^{R}(0) + \left\langle \sigma_{xy}^{R}(t) \sigma_{xy}^{V}(0) \right\rangle \right\rangle,$$
(6)

where x is the velocity direction, y is the velocity gradient direction, γ is the step strain magnitude, and V is the volume of the system. It should be noted that only the stress from main-chain springs is utilized to obtain G(t) in the original work by Likhtman (i.e., $G(t) = (V/k_BT) \rangle \sigma_{xy}^R(t) \sigma_{xy}^R(0) \int_{t}^{37} dt dt$. However, this G(t) deviates from the relaxation modulus computed by the relaxation after a small step strain, $\sigma_{xy}^R(t)/\gamma$, as explained by Ramírez and coworkers. We note that the virtual stress contribution is not more than around 25% of the main-chain contribution, and shows similar dependence on time as the main chain contribution under shear flow and is negligibly small under extensional flow (for more detail, please see Sec. S1 in the supplementary material). Thus, because of the rather long runs with small Δt values needed to adequately resolve the virtual-spring contribution and its rather weak effect, we use only the main-chain stress $\sigma_{\alpha\beta}^R$ to compute the nonlinear rheological properties.

Breakage and rejoining events are included in our method as done in our previous study;³⁶ that is, we use the reversible scission scheme and do not consider the end-interchange and the bond-interchange schemes. To incorporate these events, we introduce the probability P_{break} that a breakage event occurs for any micelle among all micelles during each time step:

$$P_{\text{break}}^{\text{eq}} = 1 \quad \exp \left(-\frac{\Delta t}{\Delta t_{\text{break}}^{\text{eq}}} \right)$$
 (7)

where Δt is the simulation time step size, and $\Delta t_{\rm break}^{\rm eq}$ is the average time between breakage events at equilibrium. In this study, a *rejoining* event occurs during each time step with probability $P_{\rm rejoin}$ that is the same as $P_{\rm break}^{\rm eq}$ over all time steps even under flow. At each simulation time step, breakage and rejoining events independently occur with the probabilities of $P_{\rm break}^{\rm eq}$ and $P_{\rm rejoin}$, respectively. Thus, the number of micelles $N_{\rm chain}(t)$ fluctuates in time. (It should be noted that the breakage probability is increased under strong extensional flow due to stress-induced micelle breakage, as explained in Sec. II B.) The average breakage time per chain with average length at equilibrium or

under weak flow, $\bar{\tau}_{\text{break}}^{\text{eq}}$, can be defined using $\Delta t_{\text{break}}^{\text{eq}}$ as

$$\bar{\tau}_{\text{break}}^{\text{eq}} = \Delta t_{\text{break}}^{\text{eq}} \rangle N_{\text{chain}}$$
(8)

where $N_{\rm chain}$ is the average number of WLM chains in the system. The dimensionless breakage time, ζ , is defined using $\bar{\tau}_{\rm break}^{\rm eq}$ as

$$\zeta \le \frac{\bar{\tau}_{\text{break}}^{\text{eq}}}{\bar{\tau}_{\text{rep}}},$$
(9)

where $\bar{\tau}_{rep} \leq 3 \rangle Z_{tube} \sqrt[3]{\tau_e}$ is the pure reptation time in the absence of other relaxation mechanisms of a micelle of average number of entanglements $\rangle Z_{tube}$ and $\tau_e \leq (N_e^{tube})^2 \tau_0/(3\pi^2)$ is the Rouse time of the chain segment between entanglements.⁴⁵

The assumptions regarding breakage/rejoining events are as follows. When a breakage event occurs at a certain simulation time step, a randomly selected main-chain bead is chosen to be a breakage point. At the breakage point, the chosen bead is duplicated, and these two beads are made the new ends of the resulting chains, as can be seen in Fig. 1. Since beads are inertialess, there is no fundamental problem with adding a bead. For a rejoining event, any two micelles can fuse with equal probability. That is, we assume the rejoining probability does not depend on micelle length, and employ a mean-field approach that does not track the relative positions of micelles. Before and after breakage and rejoining events, configurations of main chains and slip-springs and pairing information of slip-links remain the same. To reduce computational costs, we impose upper and lower bounds on $N_{\text{chain}}(t)$, $N_{\text{chain}}^{\text{max}}$ and $N_{\text{chain}}^{\text{min}}$, respectively. Additionally, we maintain upper and lower bounds on $N^{(i)}(t)$ by introducing the maximum and minimum numbers of springs per chain, $N_{\text{max}}^{\text{max}}$ and $N_{\text{min}}^{\text{min}}$, respectively.

B. Stress-Induced Micelle Breakage

Thus far, we have explained the case where the breakage and rejoining times are assumed to be constant, which is valid at equilibrium or under weak flow. Extensional flow experiments by FiSER¹³ for the CTAB/NaSal system suggest that a micelle will break when the extensional stress per micelle reaches around $3.6*10^5$ Pa. ⁴⁶ This stress is about 10^4 times larger than the experimental plateau modulus of $G_N^0 \simeq 10$ Pa for the CTAB/NaSal system. ¹³ Under strong extensional flow, the extensional stress obtained from the micelle slip-spring model is expected to become higher than the micelle breakage stress and stress-induced micelle breakage (SIMB) might become evi-

dent. To accurately model the nonlinear rheology under strong extensional flow, we address the effect of SIMB in this study.

There are several ways to address SIMB in our micelle slip-spring model. A simple way is to set the threshold stress for micelle breakage over which the micelles break. The threshold stress can be estimated from experimental data of extensional stress before rupture. ¹³ However, the experimental threshold stress might be so high that all micelles break very fast. More realistically, under high stress, the micelles can be allowed to break faster than the time scale $\bar{\tau}_{\text{break}}^{\text{eq}}$ for breakage at lower stress than the threshold stress. Mandal and Larson developed the activation formula that can address the acceleration of breakage at any stress. ⁴⁶ In this paper, we use this formula to obtain the extensional rheological properties under more reasonable conditions. The average breakage time of the chain *i* can be expressed as

$$\bar{\tau}_{\text{break}} = \tau^{\equiv} \exp \left(\frac{E_{\text{sciss}}}{k_{\text{B}}T} \right)$$
 (10)

where τ^{\equiv} is the time constant and $E_{\rm sciss}$ is the scission free energy. The molecular dynamics simulations by Mandal and Larson revealed that the dimensionless scission energy $E_{\rm sciss} = E_{\rm sciss}/k_{\rm B}T$ decreases linearly with stress. Thus, $E_{\rm sciss}$ of the chain i can be expressed as

$$E_{\text{sciss}} = E_{\text{sciss}}^{\text{eq}} \quad \frac{\sigma_{\text{E}}}{\sigma_{\text{E}}^{\text{break}}},\tag{11}$$

where $E_{\rm sciss}^{\rm eq}$ is the scission energy under no external force, $\sigma_{\rm E} \leq \sigma_{\rm E}/G_{\rm N}^0$ is the normalized extensional stress per chain, and $\sigma_{\rm E}^{\rm break} \leq \sigma_{\rm E}^{\rm break}/G_{\rm N}^0$ is the normalized characteristic extensional stress of micelle breakage, which can be estimated from molecular dynamics simulations. It should be noted that $\sigma_{\rm E}^{\rm break}$ is not identical to the experimental breakage stress per micelle ($\simeq 3.6*~10^5~{\rm Pa}$ for the CTAB/NaSal system¹³), and is expected to be smaller than the experimental breakage stress per micelle for the reason mentioned above. Combining Eqs. (10) and (11), we can obtain the breakage time under extensional flow as

$$\bar{\tau}_{break} = \tau^{\equiv} \exp \left) E_{sciss}^{eq} \frac{\sigma_{E}}{\sigma_{E}^{break}} \right[$$

$$= \bar{\tau}_{break}^{eq} \exp \left(-\frac{\sigma_{E}}{\sigma_{E}^{break}} \right) \frac{\sigma_{E}}{\sigma_{E}^{break}} \left[, \right]$$
(12)

where the average breakage time at equilibrium, $\bar{\tau}_{\text{break}}^{\text{eq}}$, is expressed as $\bar{\tau}_{\text{break}}^{\text{eq}} = \tau^{=} \exp \Big) F_{\text{sciss}}^{\text{eq}} \Big(.$

We incorporate SIMB into the slip-spring model as follows. At each simulation time step, we compute the extensional stress of individual chains, which means that each chain has different

extensional stress. This is used to determine whether or not breakage occurs using Eq. (12) and a random number. Namely, the breakage probability shown in Eq. (7) is increased under strong extensional flow. In general, the tension varies along the chain with the highest tension being near the center of the chain. In this study, however, for simplicity, we use the averaged stress over the whole chain and assume that every bead of the breaking chain has an equal probability to be the breakage point. Thus, the bead at which breakage occurs is randomly selected, as done in our original micelle slip-spring model. For rejoining events, we assume that the rejoining rate retains its equilibrium value even under strong extensional flow.

C. Parameters

Simulations are carried out using dimensionless variables. Units of stress, time and length are $G_{\text{chain}} \leq c_{\text{chain}} k_{\text{B}}T$ with c_{chain} being the chain density, $\tau_0 \leq \xi b^2/k_{\text{B}}T$, and the Kuhn length b, respectively. Here, τ_0 in this study differs from the Rouse time of a single Kuhn segment by a factor of $3\pi^2$.

Basic parameter values used in this paper are the same as those in our previous study.³⁶ For slip-spring parameters, we use $N_{\rm e}^{\rm ss}=4$, $N_{\rm s}=0.5$, and $\xi_{\rm s}/\xi=0.1$, which are the same as in Likhtman's original work.³⁷ Here, a comment on the number of "entanglements" needs to be made. The average number of slip-springs introduced to reproduce the entangled polymer dynamics, $Z_{\rm ss} = N / N_{\rm e}^{\rm ss}$, is not the same as the number of entanglements, $Z_{\rm tube} = N / N_{\rm e}^{\rm tube}$, defined in the tube model. Here, $N_{\rm e}^{\rm tube}$ is the number of beads per entanglement. Comparing the slip-spring model with the Likhtman-McLeish tube model,⁴⁷ Likhtman found that $N_{\rm e}^{\rm tube}$? 7 gives the number of beads per entanglement when using the standard slip-spring model parameters, $N_{\rm e}^{\rm ss}=4$ and $N_{\rm s}=0.5.^{37}$ (More precisely, $N_{\rm e}^{\rm tube}$ with and without CR is $N_{\rm e}^{\rm tube}=6.7$ and 5.7, respectively.⁴⁸) Thus, we use $N_{\rm e}^{\rm tube}=7$ to determine the number of entanglements per chain $Z_{\rm tube}$.

The Fraenkel parameters for main chain springs and slip-springs are both set to $K = K_{\rm ss} = 10^2$ for all simulations. The Fraenkel parameter is arbitrary as long as it is large enough to prevent spring stretch. We chose the above value because it accomplishes this without excessive computational cost required when employing very large Fraenkel parameter values. Our choice of $K = K_{\rm ss} = 10^2$ is of the same order as used in several other studies, ^{49–51} while larger values were employed in one particular study. ⁵² The simulation time step Δt is kept less than $10^{-3}\tau_0$. A Δt value smaller than $10^{-3}\tau_0$ is required to accurately obtain the stress under strong shear and ex-

tensional flow. For a shear rate range of $\dot{\gamma} > \lambda \tau_R$, where $\dot{\gamma}$ is the shear rate and $\lambda \tau_R$ is the average Rouse time defined as $\lambda \tau_R \leq (\lambda N + 1)^2 \tau_0/(6\pi^2)$, we set the time step less than the value of $\lambda \tau_R$. Here, in typical simulations, the time step size should be set to be inversely proportional to the strain rate so that the strain increment in each time step is constant. Furthermore, even for the same strain rate, we used a smaller time step in extensional flow than in shear flow. Due to the computational cost, we examined the time step size range of $\lambda t \sim 10^{-5} \tau_0$. As discussed later in Sec. III C, the smallest time step size $\lambda t = 10^{-5} \tau_0$ might not be enough to prevent overstretch under extension. Nevertheless, we confirmed that the λt values used in this study are small enough to that the stress from main chains σ^R does not show significant divergence. We show the effect of changing the time step size in Fig. S2 in the supplementary material.

For breakage and rejoining events, $\Delta t_{\text{break}}^{\text{eq}}$ is an input parameter for the simulation that is obtained from the micelle average breakage time $\bar{\tau}_{\text{break}}^{\text{eq}}$ at equilibrium from Eq. (8). To compare results from slip-spring simulations with those from other models or experiments, it is convenient to use the dimensionless breakage time ζ which can be computed from Eq. (9) once $\bar{\tau}_{\text{break}}^{\text{eq}}$ and $\bar{\tau}_{\text{rep}}$ are obtained.

In this study, we mainly set the average number of chains in the system to $\rangle N_{\text{chain}} = 2000$. For several extensional simulations with large extensional strain rates, which require a small Δt , we set $\rangle N_{\text{chain}} = 1000$. Under strong extensional flow, since the fluctuation in the extensional stress becomes small, we can safely use the smaller number of chains. We set the maximum and minimum numbers of springs to $N^{\text{max}} = 4 \rangle N$ and $N^{\text{min}} = 2$ in all simulations. The total number of micelles $N_{\text{chain}}(t)$ without SIMB is allowed to change within the range of $0.95 \rangle N_{\text{chain}} \geq N_{\text{chain}}(t) \geq 1.05 \rangle N_{\text{chain}}$. The above values are the same as in our previous study. We have checked the effect of changing the ranges of $N^{(i)}(t)$ and $N_{\text{chain}}(t)$, and confirmed that expansion of these ranges has little effect on G(t). On the other hand, there is no upper limit to $N_{\text{chain}}(t)$ for the simulations with SIMB.

D. Giesekus Model

Since the experimental shear rheological properties of WLM solutions can be successfully fitted by the Giesekus model,^{8,9} we will see the Giesekus model can also fit the micelle-slip-spring simulation results. If we can systematically map micelle parameters of the slip-spring model (e.g., the number of entanglements and the breakage rate) onto a nonlinear parameter appearing in the

Giesekus model, physical insights could thereby be indirectly incorporated into macroscopic (inhomogeneous) flow simulations, which might give better understanding of inhomogeneous flows of WLM solutions and how they depend on micellar parameters, such as the breakage rate, rather than merely on the phenomenological nonlinear parameter of the Giesekus model.

We briefly explain the Giesekus model and its steady state solutions under shear and extensional flows. The Giesekus model is a well-known phenomenological constitutive equation, which for mode p ($1 \ge p \ge N_{\text{mode}}$) is expressed as

$$\tau_p \overset{\triangledown}{\sigma}_p + (\sigma_p \quad G_p \mathbf{I}) + \alpha^G \underbrace{)} \frac{\sigma_p}{G_p} \quad \mathbf{I} \left[\times (\sigma_p \quad G_p \mathbf{I}) = \mathbf{0}, \right]$$
(13)

where σ_p is the stress for mode p, $\overset{\nabla}{\sigma}_p$ is the upper convected derivative defined as $\overset{\nabla}{\sigma}_p = \dot{\sigma}_p \quad \sigma_p \times \kappa^+ \quad \kappa \times \sigma_p$ with $\dot{\sigma}_p$ being the time derivative of σ_p and κ the velocity gradient tensor, α^G is the anisotropic parameter, which is the same for all modes,⁵⁴ I is the unit tensor, and τ_p and G_p are the relaxation time and modulus for mode p, respectively. Here, τ_p and G_p are determined by the multi-mode Maxwell model fitting of the relaxation modulus. The total stress σ is $\sigma = \sum_{p=1}^{N_{\text{mode}}} \sigma_p$.

In shear flow, the steady shear viscosity for mode p, η_p , is written as⁵⁵

$$\frac{\eta_p}{\eta_{0,p}} = \frac{(1 \quad f_p^{S}[\dot{\gamma}, \alpha^G])^2}{1 + (1 \quad 2\alpha^G) f_p^{S}[\dot{\gamma}, \alpha^G]},\tag{14}$$

where $\eta_{p,0}$ (= $G_p \tau_p$) is the zero shear viscosity for mode p, and $f_p^S[\dot{\gamma}, \alpha^G]$ is the function defined as

$$f_p^{\mathbf{S}}[\dot{\gamma}, \alpha^{\mathbf{G}}] = \frac{1 \quad g_p^{\mathbf{S}}[\dot{\gamma}, \alpha^{\mathbf{G}}]}{1 + (1 \quad 2\alpha^{\mathbf{G}})g_p^{\mathbf{S}}[\dot{\gamma}, \alpha^{\mathbf{G}}]},\tag{15}$$

with

Here, $\dot{\gamma}$ is the shear rate. Under extensional flow, the steady extensional viscosity for mode p, $\eta_{E,p}$, is

$$\frac{\eta_{\mathrm{E},p}}{3\eta_{0,p}} = \frac{1}{6\alpha^{\mathrm{G}}} 3 + f_p^{\mathrm{E}}[\dot{\boldsymbol{\varepsilon}}, \alpha^{\mathrm{G}}] + g_p^{\mathrm{E}}[\dot{\boldsymbol{\varepsilon}}, \alpha^{\mathrm{G}}]$$
(17)

with

$$f_p^{E}[\dot{\varepsilon}, \alpha^{G}] = \frac{1}{\tau_p \dot{\varepsilon}} \left\{ 1 \quad 4 \quad 1 \quad 2\alpha^{G} \left\{ \tau_p \dot{\varepsilon} + 4 \left(\tau_p \dot{\varepsilon} \right)^2 \right\}^{1/2} \right\}$$
 (18)

and

$$g_p^{E}[\dot{\varepsilon}, \alpha^{G}] = \frac{1}{\tau_p \dot{\varepsilon}} \left\{ 1 + 2 \ 1 \ 2\alpha^{G} \left\{ \tau_p \dot{\varepsilon} + (\tau_p \dot{\varepsilon})^2 \right\}^{1/2} \right\},$$
 (19)

where $\dot{\varepsilon}$ is the extension rate. The anisotropic parameter α^G is determined by fitting steady shear or extensional viscosity data.

E. Phan-Thien/Tanner Model

In addition to the comparison of slip-spring simulation results with predictions of the Giesekus model, we will test another common constitutive equation, namely the Phan-Thien/Tanner (PTT) model. ^{53,56} The PTT model is expressed as

$$\tau_p \overset{\square}{\sigma}_p + Y \left] \operatorname{Tr} \right) \sigma_p \quad \frac{G_p^{\circ}}{a^2} I \left[\left\{ \right\} \sigma_p \quad \frac{G_p^{\circ}}{a^2} I \left[\right] = 0, \right]$$
(20)

where σ_p is the Gordon-Schowalter convected derivative defined as $\sigma_p = \dot{\sigma}_p$ $\sigma_p \not \approx 1$ $\kappa \not = \sigma_p + (1-a)(\sigma_p \not \approx D + D \not = \sigma_p)$ with a being the parameter describing a slippage of the strand and $D = (\kappa + \kappa^+)/2$ being the strain rate tensor, Y is a function of the term in brackets that depends on the average conformation of the polymer chains through the trace of the stress tensor as indicated, and G_p° is the modulus defined as $G_p^\circ = a^2 G_p$. In this study, we set a = 1 to avoid unphysical oscillations produced by the Gordon-Schowalter convected derivative under shear flow. Thus, σ_p and σ_p reduce to σ_p and σ_p are determined by the multi-mode Maxwell model fitting of σ_p .

Two functional forms for the dependence of Y on conformation have been suggested, namely a linear function and an exponential function. The difference between the two forms is evident in the steady extensional viscosity as a function of the extensional rate. For the linear function, the extensional viscosity shows extension hardening followed by a high-extension-rate plateau. For the exponential function, the extensional viscosity shows extension hardening followed by extension thinning. Since typical experimental extensional viscosities obtained by the opposed jet device show extension hardening followed by extension thinning, $^{15-17}$ we use the exponential function expressed as

$$Y\left[\operatorname{Tr}\left(\boldsymbol{\sigma}_{p} \quad G_{p}\boldsymbol{I}\right)\right] = \exp \left\{\frac{\boldsymbol{\alpha}^{\operatorname{PTT}}}{G_{p}}\operatorname{Tr}\left(\boldsymbol{\sigma}_{p} \quad G_{p}\boldsymbol{I}\right)\right\},\tag{21}$$

where α^{PTT} is the nonlinear parameter in the PTT model. As in the Giesekus model, the nonlinear parameter α^{PTT} is the same for all modes. That is, we use a single nonlinear parameter α^{PTT} to fit the slip-spring data. When we use the exponential function shown in Eq. (21), the steady shear viscosity can be expressed as⁵⁷

$$\frac{\eta_p}{\eta_{0,p}} = \frac{1}{2\tau_p \dot{\gamma}} \frac{W[4\alpha^{\text{PTT}} \tau_p^2 \dot{\gamma}^2]}{\alpha^{\text{PTT}}} \left\langle {}^{1/2}, \right\rangle$$
 (22)

where W[x] is the Lambert W function. Since no analytical solution exists for the steady-state solution under uniaxial extensional flow, we numerically solve Eq. (20) to obtain steady extensional viscosity.

Finally, in this study, we do not use the popular VCM model to fit the slip-spring data because the VCM model is a two species dumbbell model, whose the linear viscoelastic behavior is expressed by the superposition of the two relaxation times. Thus, it does not give a good fit to the linear viscoelastic data of the slip-spring model. In addition, the VCM model is based on dilute dumbbells with no entanglement effects, making it physically unsuitable to describe the shear thinning produced by entanglements in entangled WLM solutions.

III. RESULTS AND DISCUSSION

A. Linear Viscoelasticity

We first show the linear viscoelastic (LVE) properties of the micelle-slip-spring model with the Fraenkel spring potential. Before calculating the LVE data, all WLM chains in the ensemble are equilibrated without flow for a time $t_{\rm eq}$. The relaxation time needed to equilibrate the micelles $t_{\rm eq}$ depends on the dimensionless breakage time ζ as $t_{\rm eq} \sim 2(\bar{\tau}_{\rm rep}\bar{\tau}_{\rm break}^{\rm eq})^{1/2}$ for $\zeta < 1$ or $t_{\rm eq} \sim 2\bar{\tau}_{\rm rep}$ for $\zeta \sim 1$. Here, $(\bar{\tau}_{\rm rep}\bar{\tau}_{\rm break}^{\rm eq})^{1/2}$ is the theoretically estimated longest relaxation time in the fast-breakage limit by Cates.²⁵

In our previous paper,³⁶ we presented G(t) data from the slip-spring model using Hookean springs obtained by relaxation after a small step shear strain. We here re-compute G(t) for the Fraenkel springs from equilibrium simulations using the Green-Kubo formula. We carry out this re-calculation for the following two reasons. First, G(t) of Fraenkel springs is slightly different from that of Hookean springs with the same numbers of main chain springs and slip-springs. (For more detail, please see Fig. S3 in the supplementary material). Since G(t) is a small-strain property, predictions of it from the slip-spring model with Fraenkel springs should converge to those with Hookean springs when the Fraenkel spring constant is very large and there are enough short Fraenkel springs to recover Hookean behavior. To simulate with a large Fraenkel spring constant, a very small Δt is required and thus it takes a long simulation time to obtain reliable results. Even with this, since the nonlinearity arising from the Fraenkel potential exists even in the small strain region, it is difficult to obtain an accurate G(t) from relaxation after a small step

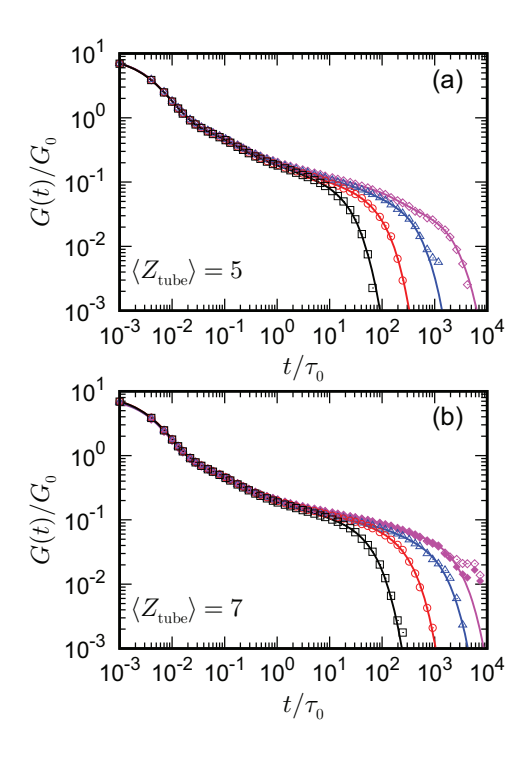


FIG. 2. Relaxation modulus G(t) computed from the slip-spring model by Green-Kubo formula for (a) $\langle Z_{\text{tube}} \rangle = 5$ and (b) 7 at four dimensionless breakage times $\zeta = 0.01$ (black), 0.1 (red), 1 (blue), and 10 (magenta) with solid lines giving fits by the multi-mode Maxwell model. In (b), filled symbols are the calculation of the correlation function (cf. Eq. (6)) for the time duration $t_{\text{LVE}} = (t_{\text{total}} \quad t_{\text{eq}}) = 6 * 10^4 \tau_0$, and open symbols are for $t_{\text{LVE}} = 1 * 10^5 \tau_0$.

shear strain, as also reported by Lin and Das who compared the relaxation behavior of Hookean and Fraenkel springs.⁴⁹ For more detail, please see Sec. S4 in the supplementary material. Thus, we use the Green-Kubo formula to obtain accurate G(t) data. To compute G(t), we utilize Eq. (6) and the multiple-tau correlator for efficient calculations.⁵⁸

Figure 2 shows the relaxation modulus G(t) for (a) $\rangle Z_{\text{tube}} = 5$ and (b) 7 at four dimensionless breakage times $\zeta = 0.01$ (black), 0.1 (red), 1 (blue), and 10 (magenta). Here, G_0 is the modulus defined as $G_0 = \rangle N$ \int_{chain} utilized as the unit of stress in Likhtman's work. After the equilibrium simulation for the time period t_{eq} , we performed the simulation with $\kappa = 0$ for a time duration $t_{\text{LVE}} = (t_{\text{total}} \quad t_{\text{eq}}) = 1 * 10^5 \tau_0$ to compute G(t), where t_{total} is the total simulation time. This t_{LVE} is at least 50 times longer than the longest relaxation time (cf. Table S1 and S2 in the supplementary material). It should be noted that G(t) for $\langle Z_{\text{tube}} \rangle = 7$ and $\zeta = 10$ shown in Fig. 2(b) for $t \gtrsim 3000\tau_0$ seems not to be converged due to the limited computational time. Thus, only the G(t) data for $t \lesssim 3000\tau_0$ is utilized in later analysis. From Fig. 2, the short-time relaxation behavior wherein

G(t) exceeds unity for $t \lesssim 10^{-2} \tau_0$ is absent for Hookean chains, for which G(t) normalized as described above approaches unity at short times. The rise of G(t) above unity at short time is due to the Fraenkel potential used in this study, as noted in the literature. Horeover, relaxation behavior in the relatively short time region $t \lesssim \tau_0$ is almost identical for all breakage rates. This is because the breakage time is much larger than the unit time of the system. The difference between different breakage times can be seen in the long-time region. As expected, the relaxation becomes slower with increasing breakage time (i.e., decreasing breakage rate). The G(t) results obtained from slip-spring simulations with the Fraenkel potential are then fitted by the multi-mode Maxwell model $G(t) = \sum_p G_p \exp(-t/\tau_p)$ where τ_p and G_p , respectively, are the relaxation time and strength for mode p. The fitting results are shown in Fig. 1 with solid lines. We will use the set of parameters τ_p and τ_p are the relaxation time and strength for mode τ_p and τ_p are shown in Fig. 1 with solid lines. We will use the set of parameters τ_p and τ_p and τ_p and τ_p and τ_p are the relaxation time and strength for mode τ_p and τ_p are the relaxation time and strength for mode τ_p and τ_p are the relaxation time and strength for mode τ_p and τ_p are the relaxation time and strength for mode τ_p and τ_p and τ_p are the relaxation time and strength for mode τ_p and τ_p are the relaxation time and strength for mode τ_p and τ_p are the relaxation time and strength for mode τ_p and τ_p are the relaxation time and strength for mode τ_p and τ_p are the relaxation time and strength for mode τ_p are the relaxation time and strength for mode τ_p and τ_p are the relaxation time and strength for mode τ_p and τ_p are the relaxation time and τ_p are the relaxation time and τ_p are t

B. Rheological Properties under Shear Flow

Next, we investigate nonlinear shear rheological properties. In all of slip-spring simulations in this subsection, which focuses on shear properties, the breakage and rejoining times are assumed to retain constant values (i.e., $\bar{\tau}_{break} = \bar{\tau}_{rejoin} = \bar{\tau}_{break}^{eq}$) so that the breakage rate does not depend on configuration or stress. Extensional flow experiments ¹³ for the CTAB/NaSal system suggest that a micelle will break when under a stress of around $3.6*10^5$ Pa, roughly consistent with molecular dynamics simulations. ⁴⁶ This scission stress is high enough that micelle scission is likely to occur only under strong *extensional* flow, and not under *shear* flow. The effect of stress-induced micelle breakage at the high-stress level under shear flow will be addressed in our future work, if necessary.

Figure 3 shows the steady shear viscosities $\eta \leq \sigma_{xy}^R/\dot{\gamma}$ for three dimensionless breakage times (a) $\zeta = 0.01$, (b) 0.1 and (c) 1. The slip-spring simulation results with $\rangle N = 35$ springs and $\rangle Z_{\text{tube}} = 5$ entanglements are plotted with symbols. As can be seen in Fig. 3, the micelle slip-spring model can reproduce shear thinning due to the effect of the entanglement constraint. Here, it should be noted that the shear-rate dependencies of the shear viscosity of WLM and polymer solutions are characterized by a power law, i.e., $\eta \propto \dot{\gamma}^n$, but with different exponents. The exponent n for WLM solutions is typically around n = 1, whereas for nearly monodisperse polymer solutions it is typically around n = 0.8.59 This is an important difference since the power law of $\eta \propto \dot{\gamma}^{-1}$ in WLM solutions, which corresponds to a stress plateau in the steady-state flow curve, is

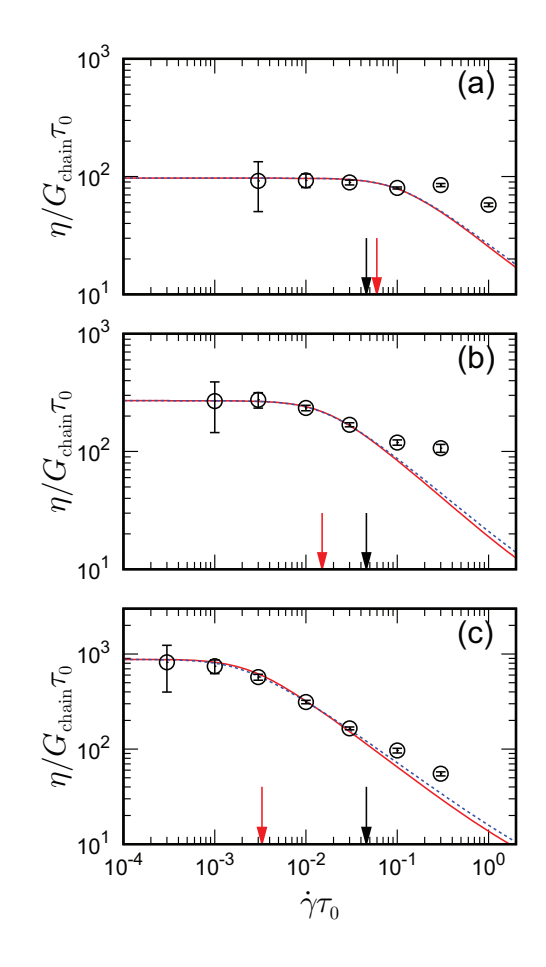


FIG. 3. Steady shear viscosities at three dimensionless breakage times (a) $\zeta = 0.01$, (b) 0.1, and (c) 1. Slip-spring simulation results for N = 35 (i.e., $Z_{\text{tube}} = 5$) are presented with symbols, fitting results by the Giesekus model are shown with red solid lines, and those by the PTT model with blue dotted lines. The black and red arrows are the inverse of the average Rouse time $T_{\text{R}} = 1$ and the inverse of the average relaxation time $T_{\text{R}} = 1$, respectively. Here, the error bars show the standard deviations, which are less than the symbol size except at the lowest shear rate.

responsible for shear banding. In Fig. 3, however, the number of entanglements and the shear rate ranges are too small to observe this characteristic exponent for WLMs (n / 1). To investigate the higher shear rate region, the missing mechanisms here (e.g., the entanglement loss under flow) should be incorporated into the micelle slip-spring model. Although the limiting case in which there is flow-induced loss of entanglements but no regeneration of them is examined in Sec. III D, consideration of a better slip-spring regeneration algorithm under flow is deferred to a future work. Red solid and blue dotted lines in Fig. 3 are the fitting results for $\dot{\gamma} \rangle \tau_R \lesssim 1$, where $\rangle \tau_R$ is the average Rouse relaxation time, by the Giesekus model (cf. Eqs. (14) \simeq (16)) and the PTT model

TABLE I. Nonlinear parameters for the Giesekus model α^G and the Phan-Thien/Tanner model α^{PTT} .

ζ	$lpha_{ m shear}^{ m G}$	$lpha_{ m ext}^{ m G}$	$lpha_{ m shear}^{ m PTT}$	$lpha_{ m ext}^{ m PTT}$
0.01	0.036	0.024	0.054	0.010
0.1	0.11	0.037	0.17	0.013
1	0.33	0.11	0.56	0.021

(cf. Eq. (22)), respectively. The nonlinear parameter appearing in each constitutive equation is the same for all modes. Thus, a single nonlinear parameter is used in each constitutive model to fit the slip-spring data. We observe that the steady shear viscosities for $\dot{\gamma} \rangle \tau_R \lesssim 1$ obtained by the slip-spring model can be successfully reproduced by both the Giesekus and the PTT models with nonlinear parameter values summarized in Table I. On the other hand, the slip-spring simulation data for $\dot{\gamma} \rangle \tau_R > 1$ are not well reproduced by the constitutive models. Here, we note that there is no physical reason that a near perfect agreement should be obtained since the constitutive models used here are phenomenological, and are not microstructurally-based. Almost the same trend can be observed for the case of $\rangle N = 49$ springs and $\rangle Z_{\text{tube}} = 7$ entanglements, as shown in Fig. S4(a) in the supplementary material.

Figure 4 shows transient shear viscosities $\eta^+(t) \le \sigma_{xy}^R(t)/\dot{\gamma}$ for (a) $\zeta = 0.01$, (b) 0.1, and (c) 1. Slip-spring simulation results with N = 35 (i.e., N = 35 (i.e., N = 35) are plotted with symbols. Here, the same color in each figure means the same strain rate. The linear viscosity growth function $\eta_0^+(t)$ computed from the LVE data is shown with the black dotted line. The stress overshoot shown by the slip-spring model predictions qualitatively matches that seen in experiments. For the high strain rate region N = 10, the shear viscosity exceeds the linear viscosity growth function, thus showing a "hardening" prior to the stress overshoot. This may be related to the nonlinearity of the chain extension at high strain rates, because of the small number of Kuhn steps per spring in our model. This hardening behavior under strong shear, which is attributed to the finite extensibility of springs, is observed in experiments for CTAB/NaSal systems, as reported by Inoue and coworkers. Similarly, stiff entangled polymers are known to produce strain hardening in shear. This strain hardening in our model will likely weaken if strain-induced entanglement loss at high shear rates is included. As can be seen in the solid lines of Fig. 4, the transient shear viscosities, including the stress overshoots seen in N = 100 N = 100

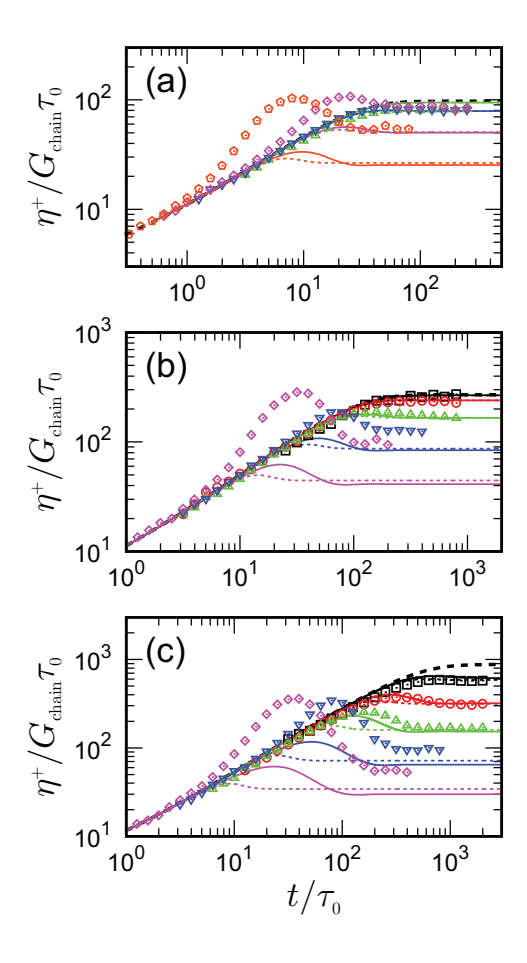


FIG. 4. Transient shear viscosities $\eta^+(t)$ for (a) $\zeta=0.01$, (b) 0.1, and (c) 1. Slip-spring simulation results with $\rangle N = 35$ and $\rangle Z_{\text{tube}} = 5$ are plotted with symbols. Shear rates are $\dot{\gamma}\tau_0 = 3*10^{-3}$ (black squares), $1*10^{-2}$ (red circles), $3*10^{-2}$ (green triangles), $1*10^{-1}$ (blue reverse triangles), $3*10^{-1}$ (pink diamonds), and 1 (orange pentagons). The Weissenberg number (Wi_{shear}) ranges in each figure are (a) $0.5 \simeq 17$, (b) $0.2 \simeq 20$, and (c) $0.3 \simeq 90$, where Wi_{shear} is defined as $Wi_{\text{shear}} \leq \dot{\gamma} \rangle \tau$ with $\langle \tau \rangle = (\sum_{p=1}^{N_{\text{mode}}} G_p \tau_p^2)/(\sum_{p=1}^{N_{\text{mode}}} G_p \tau_p)$ being the average relaxation time. The linear viscosity growth function $\eta_0^+(t)$ computed from the LVE data is shown with the black bold dotted line. The predictions by the Giesekus and the PTT models are plotted with solid and dotted lines, respectively.

in Fig. 3. While the steady-state slip-spring simulation data for $\dot{\gamma}\rangle\tau_R\lesssim 1$ are reasonably captured by the PTT model as shown in Fig. 3, the transient shear viscosity predictions are poorer than those of the Giesekus model in that the stress overshoot in the PTT model is less prominent than in the slip-spring model. However, the hardening behavior seen in $\dot{\gamma}\rangle\tau_R\gg 1$ is not reploduced by these constitutive models, where the effect of finite extensibility is not addressed. Almost the same trend can be observed for the case of $\rangle N = 49$ springs and $\rangle Z_{\text{tube}} = 7$ entanglements, as

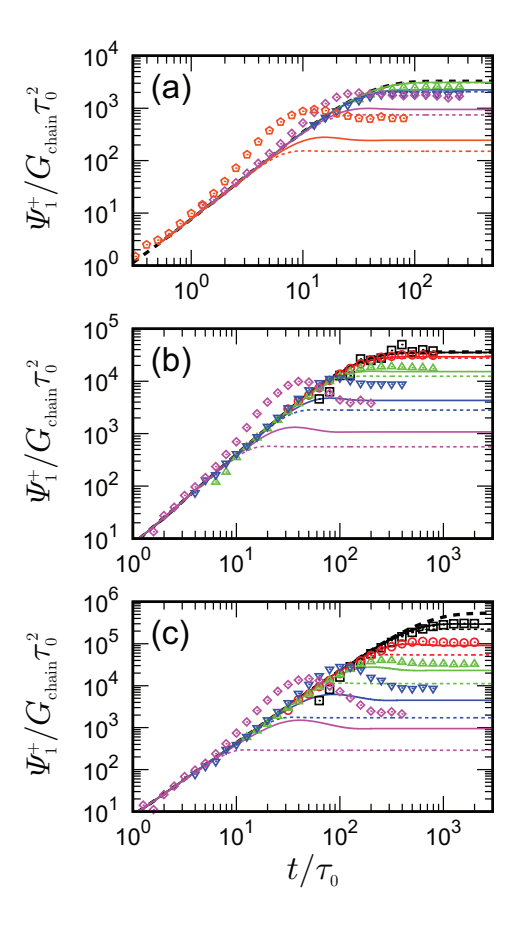


FIG. 5. The same as Fig. 4, except for transient normal stress coefficients $\Psi_1^+(t)$. The first normal stress growth function $\Psi_{1,0}^+(t)$ computed from the LVE data is shown with the black bold dotted line.

shown in Fig. S5(b) in the supplementary material. Better predictions by the PTT model might be obtained by setting the slip-parameter in the Gordon-Schowalter convected derivative to $a \neq 1$. However, doing so produces unphysical stress oscillations under shear flow, which are not seen in current slip-spring simulations.

Figure 5 shows normal stress coefficients $\Psi_1^+(t) \leq N_1(t)/\dot{\gamma}^2 = \frac{1}{3}\sigma_{xx}^R(t)$ $\sigma_{yy}^R(t)\langle/\dot{\gamma}^2 \text{ for (a) }\zeta = 0.01$, (b) 0.1, and (c) 1 with the same parameters as those in Fig. 4. The first normal stress growth function $\Psi_{1,0}^+(t)^{53}$ computed from the LVE data is also shown with the black dotted line. The Giesekus model (solid lines) can reproduce both the transient and the steady state data predicted by the slip-spring model for $\dot{\gamma}\rangle\tau_R \lesssim 1$. However, as is the case for the transient shear viscosity, the PTT model predictions (dotted lines) for both the transient and steady normal stress coefficients deviate from the slip-spring simulation data for $\dot{\gamma}\rangle\tau_R \lesssim 1$. Moreover, both constitutive models cannot reproduce $\Psi_1^+(t)$ for $\dot{\gamma}\rangle\tau_R > 1$. Almost the same trend can be observed for the case of $\lambda N = 49$ springs and $\lambda N = 49$ s

material.

From the comparison of slip-spring simulation data with the Giesekus and PTT models in Figs. 4 and 5, the Giesekus model matches better the slip-spring data than does the PTT model under moderate shear flow where the chains do not show significant stretch. Since experimental studies show that the Giesekus model can also reproduce the shear rheological data of WLM solutions, ^{8,9} the micelle slip-spring model will also be in qualitative agreement with the experimental shear data. We note that the strain hardening behavior seen in both the slip-spring model and the experiments for the CTAB/NaSal system¹² is not reproduced by the Giesekus model. Thus, we can conclude that a constitutive model that can predict rheological properties under strong shear flow has not yet developed.

In experiments of shear-rate regions showing shear thinning, flows of typical WLM solutions show shear banding. 22,23 To predict shear banding, spatially-dependent simulations are required. Such simulations with the micelle-slip-spring model incur excessive computational costs. Since the slip-spring model predictions for $\dot{\gamma}$ $\rangle \tau_R \lesssim 1$ are well reproduced by the Giesekus model, the latter can be used for such spatially-dependent simulations. This will be the goal of our future research whose aim is to use slip-spring simulations to choose and tune a constitutive model to produce similar responses in flows such as shear, extensional, and mixed flows, thus validating it for use in more complex flows.

C. Rheological Properties under Extensional Flow

Next, we investigate uniaxial extensional rheological properties obtained by the micelle slip-spring model again with Fraenkel springs. As for shear flow, we first omit stress-induced micelle breakage (i.e., $\bar{\tau}_{break} = \bar{\tau}_{break}^{eq}$), and show the basic properties of the micelle slip-spring model under extensional flow. However, as discussed above, experiments¹³ and recent molecular dynamics simulations⁴⁶ reveal that stress-induced micelle breakage is expected when the stress becomes several orders of magnitude larger than the plateau modulus. This might be the case at the high extensional rates examined in this study. Thus, we will also test the effect of stress-induced micelle breakage (SIMB) for several conditions.

Figure 6 shows steady extensional viscosities $\eta_E = \sigma_E/\dot{\epsilon}$ normalized by the zero shear viscosity η_0 for three dimensionless breakage times (a) $\zeta = 0.01$, (b) 0.1, and (c) 1 with the steady extensional stress σ_E defined by $\sigma_E = \sigma_{xx}^R (\sigma_{yy}^R + \sigma_{zz}^R)/2$. Slip-spring simulation results without

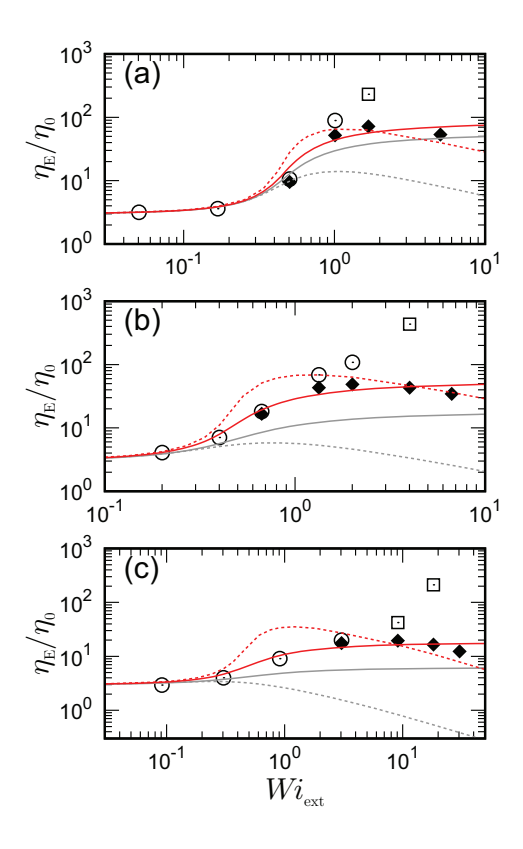


FIG. 6. Steady extensional viscosities at three dimensionless breakage times (a) $\zeta = 0.01$, (b) 0.1, and (c) 1. Slip-spring simulation results for N = 35 (i.e., $Z_{\text{tube}} = 5$) with and without stress-induced micelle breakage are presented with filled and open symbols, respectively. Here, the simulation results showing significant spring stretch beyond the theoretical maximum value are plotted with open squares. The Giesekus and PTT model predictions with the same parameters as under shear flow are shown with gray solid and dotted lines, respectively, while those with modified nonlinear parameters for extensional flow are shown with red solid and dotted lines, respectively.

SIMB are plotted with open symbols. To compare simulation results with the experimental data, it is convenient to introduce the Weissenberg number defined as $Wi_{\text{ext}} \leq \dot{\varepsilon} \rangle \tau$, where $\rangle \tau$ is an average relaxation time defined as $\rangle \tau = (\sum_{p=1}^{N_{\text{mode}}} G_p \tau_p^2)/(\sum_{p=1}^{N_{\text{mode}}} G_p \tau_p)$. In Fig. 6, the simulation results showing significant spring stretch beyond the theoretical maximum value are plotted with open squares. Under high extensional flows, the average squared end-to-end vector for the micellar chains, $\rangle R_{\text{EE}}^2$, becomes larger than the theoretical maximum value $\rangle R_{\text{EE},\text{max}}^2 = (\rangle N b)^2$ since longer chains in the ensemble show significant stretch (for more details, please see Fig. S6 in the supplementary material). This is evident for slower breakage cases where longer chains less frequently break. There are two possible reasons for this overstretch: one is the Fraenkel spring

constant is not large enough, the other is Δt values ($\Delta t \simeq 10^{-5} \tau_0$ for high extensional rates) are not small enough. However, it is not practical to employ larger Fraenkel parameters or smaller Δt values due to the large computational cost. In the current case, however, since the number of these chains is small, the extensional stress is expected not to be much affected by these chains. This is partly supported by the fact that the extensional stress does not show significant divergence (cf. Fig. 7). In Fig. 6, we also plot with gray solid and dotted lines the predictions of the Giesekus model and PTT model, respectively, with the same nonlinear parameter as that under shear flow. From Fig. 6, we can observe that extensional viscosities from the slip-spring simulations without SIMB monotonically increase at $Wi_{\rm ext} \gtrsim 0.5$. This is a typical behavior obtained by the bead-spring models.⁵⁰ On the other hand, extensional viscosities predicted by the Giesekus and PTT models show extension thickening followed by a high Weissenberg number plateau and extension thinning, respectively. Experimentally, Walker and coworkers reported the extensional viscosities for CPyCl/NaSal solutions show extension thickening followed by extension thinning, where the increase in $\eta_{\rm E}$ occurs at $Wi_{\rm ext}^{({\rm expt})}$ / 0.7 and the maximum in $\eta_{\rm E}$ is seen at around $Wi_{\rm ext}^{({\rm expt})}$ $^{\prime}$ 4 \simeq 7. 17 Here, $Wi_{\rm ext}^{({\rm expt})}$ is obtained by multiplying experimental apparent strain rates and a terminal relaxation time $\tau_{\rm expt}$, which is evaluated by $\tau_{\rm expt}=\eta_0/G_{\rm N}^0$. While the slip-spring simulations can reasonably capture the onset of the increase in $\eta_{\rm E}$, the original slip-spring simulations without SIMB cannot reproduce extension thinning seen in experiments. Thus, there should be a missing mechanism(s) in the original micelle slip-spring model under strong extensional flow. It should be noted that the PTT model can qualitatively capture experimental extensional viscosities, i.e., extension thickening followed by extension thinning. However, the maximum in η_E becomes less prominent with increasing dimensionless breakage time.

As discussed earlier, we incorporate stress-induced micelle breakage (SIMB) to improve slip-spring predictions under strong extensional flow. To implement SIMB, the characteristic extensional stress, σ_E^{break} , appearing in Eq. (12) should be determined. This can be done with the assistance of the molecular dynamics simulation. For example, for the cetyltrimethylammonium chloride (CTAC)/NaSal system, utilizing the scission energy vs stress data shown in Fig. 6(b) of the work by Mandal and Larson and performing a linear fit (cf. Eq. (11)), we can estimate σ_E^{break} to be σ_E^{break} / $3*10^5$ Pa for the CTAC/NaSal system at the salt concentration giving the lowest breakage rate. This value is much higher than the experimental plateau modulus of CTAC/NaSal systems. It should be noted that the characteristic stress might be system dependent, and has not been systematically examined. To the best of our knowledge, for the CPyCl/NaSal system,

whose extensional properties are reported by Walker and coworkers, 17 no information to estimate the characteristic stress has been reported. Here, based on the finding that $\sigma_{\rm E}^{\rm break}$ is much higher than the plateau modulus, we assume a value much lower than estimated by Mandal and Larson, that is we take $\sigma_{\rm E}^{\rm break} = 2*10^4$ Pa which allows us to find a significant effect of SIMB on rheological properties. (Comparison to the larger value of $\sigma_{\rm E}^{\rm break}$, i.e., $\sigma_{\rm E}^{\rm break} = 1*10^5$ Pa closer to the value of Mandal and Larson, 46 giving much less extension thinning, is shown in Sec. S7 in the supplementary material.) If we assume that the experimental plateau modulus as $G_{\rm N}^0$ 10 Pa, the dimensionless characteristic extensional stress is evaluated as $\sigma_{\rm N,ss}^{\rm break}$ 12*10³. In the slip-spring model, the plateau modulus can be approximated as $G_{\rm N,ss}^0 = 0.18*0.8G_0 = 0.144G_0.48$ During simulations, we rescale the extensional stress by $G_{\rm N,ss}^0$ to compute $\sigma_{\rm E}^0$, and evaluate the breakage time by Eq. (12).

In Fig. 6, slip-spring simulation results with SIMB are plotted with filled symbols. We can observe that the extensional viscosities show the maximum at around $Wi_{\rm ext}$ / $2 \simeq 3$, which is almost the same as in the experimental results by Walker and coworkers. Here, $R_{\rm EE}$ with SIMB is smaller than, or at most slightly larger than the theoretical maximum value. As compared to the simulations without SIMB, the degree of overstretch is thus significantly suppressed (for more details, please see Fig. S6 in the supplementary material). The constitutive models using the nonlinear parameter derived from fitting shear flow (gray lines in Fig. 6) underestimate η_E obtained by the slip-spring model with SIMB (filled symbols in Fig. 6). To improve the predictions of the constitutive models, we separately fit the Giesekus and PTT models to the extensional data with SIMB of $Wi_{\rm ext} \gtrsim 1$. While we use Eqs. (17) \simeq (19) for the Giesekus model fit, an optimal PTT fit to the extensional data can be obtained by minimizing the value of $\sum_j \{(\eta_{{\rm E},j}^{\rm PTT} - \eta_{{\rm E},j})/\eta_{{\rm E},j} \langle^2,$ where j is the individual data points with different strain rates, $\eta_{\mathrm{E},j}^{\mathrm{PTT}}$ is the steady extensional viscosity of the PTT model, and $\eta_{\mathrm{E},j}$ is the steady extensional viscosity of the slip-spring model. The parameter values under extensional flow are summarized in Table I. The fitting results are shown in Fig. 6 with red lines. As can be seen in Table I, the Giesekus and PTT models with the smaller nonlinear parameter values than under shear flow give better predictions under uniaxial extensional flow. We can see that the Giesekus model can reproduce the slip-spring simulation results better than the PTT model. However, the Giesekus model cannot predict extension thinning observed in experiments and slip-spring simulations with SIMB. On the other hand, the PTT model can reproduce extension thinning, but provides poorer predictions at the onset of extension thickening. It should be noted that the Giesekus and PTT models with the nonlinear parameter determined

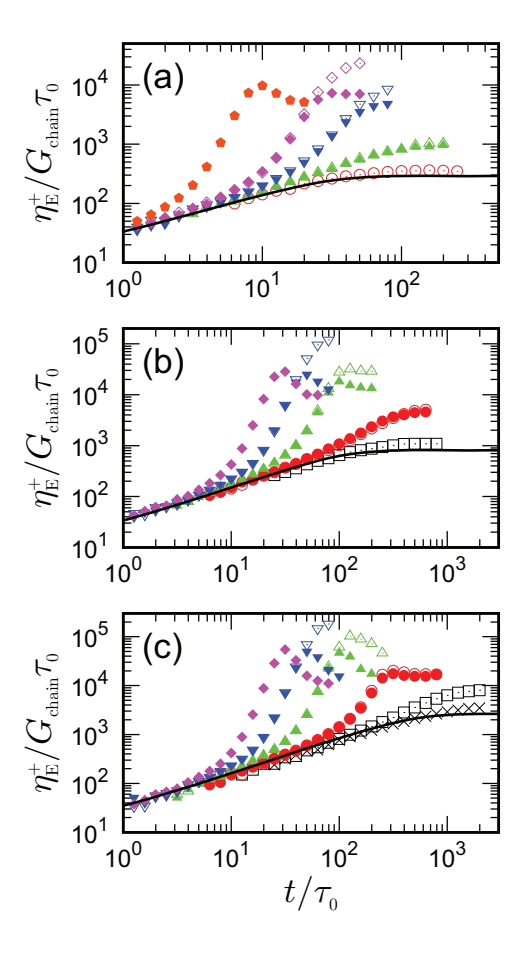


FIG. 7. Transient uniaxial extensional viscosities $\eta_{\rm E}^+(t)$ for (a) $\zeta=0.01$, (b) 0.1, and (c) 1. Slip-spring simulation results for $\rangle N_{\downarrow}=35$ and $\rangle Z_{\rm tube}_{\downarrow}=5$ with and without stress-induced micelle breakage (SIMB) are shown with filled and open symbols, respectively. Strain rates are $\dot{\epsilon}\tau_0=1*10^{-3}$ (black cross marks), $3*10^{-3}$ (black squares), $1*10^{-2}$ (red circles), $3*10^{-2}$ (green triangles), $6*10^{-2}$ (blue reverse triangles), $1*10^{-1}$ (pink diamonds), and $3*10^{-1}$ (orange pentagons). Simulation results without SIMB for the largest strain rates are not shown since these results show significant overstretch. Moreover, simulation results with SIMB for the small strain rates are not shown since SIMB only becomes significant at high stress levels, which are not reached for small strain rates. The linear viscosity growth function $\eta_{\rm E0}^+(t)$ obtained from the LVE data is presented with the black bold line.

under extensional flow give poorer predictions under shear flow than those shown in Figs. 4 and 5 (for more details, please see Fig. S8 in the supplementary material).

Figure 7 shows transient uniaxial extensional viscosities $\eta_{\rm E}^+(t)$ for (a) $\zeta=0.01$, (b) 0.1, and (c) 1. For each ζ value, $\eta_{\rm E}^+(t)$ curves of the slip-spring model with the smallest strain rate ($\dot{\varepsilon}\tau_0=1*10^{-2}$ for $\zeta=0.01$, $\dot{\varepsilon}\tau_0=3*10^{-3}$ for $\zeta=0.1$, and $\dot{\varepsilon}\tau_0=1*10^{-3}$ for $\zeta=1$) are almost

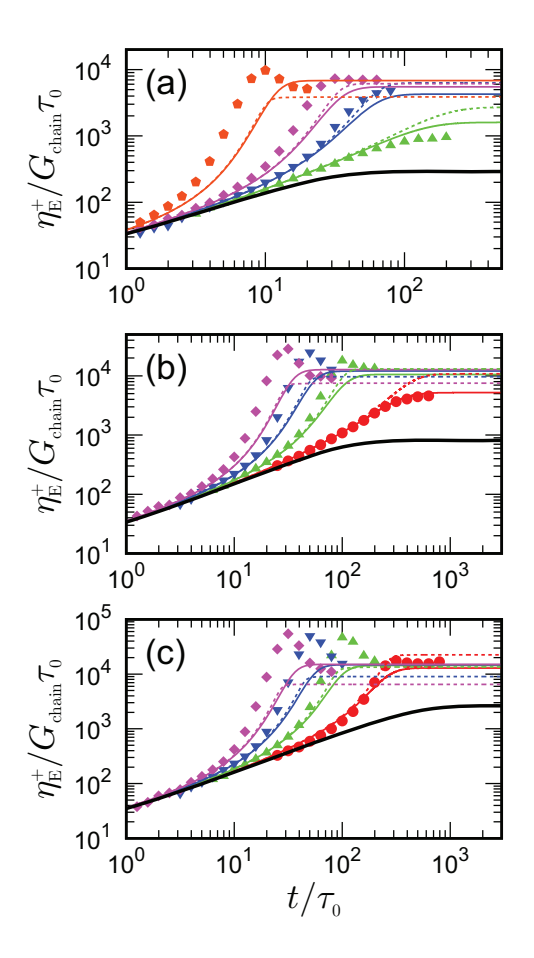


FIG. 8. Transient uniaxial extensional viscosities $\eta_{\rm E}^+(t)$ for (a) $\zeta=0.01$, (b) 0.1, and (c) 1. Slip-spring simulation results for N = 35 and $Z_{\rm tube} = 5$ with stress-induced micelle breakage are shown with filled symbols. The strain rates are the same as those in Fig. 7. The Giesekus and PTT model predictions with modified nonlinear parameters for extensional flow are shown with solid and dotted lines, respectively.

identical to η_{E0}^+ , which indicates that these strain rates are in the linear response regions. In the small strain rate region ($\dot{\varepsilon}\tau_0 \geq 3*10^{-2}$ for $\zeta=0.01$, and $\dot{\varepsilon}\tau_0 \geq 1*10^{-2}$ for $\zeta=0.1$ and $\zeta=1$), $\eta_E^+(t)$ curves with and without SIMB are almost identical, which indicates that SIMB does not affect $\eta_E^+(t)$ in the small strain rate region. In the larger strain rate region, the effect of SIMB can be detected for all ζ cases. While transient extension hardening behavior with SIMB is almost identical to that without SIMB, $\eta_E^+(t)$ with SIMB shows a maximum before reaching a steady state, which is the qualitatively different behavior from that without SIMB. As shown in Fig. 6 with filled symbols, the steady extensional viscosities show weak extension thinning.

In Fig. 8, we plot the Giesekus and PTT model predictions with modified nonlinear parameters for extensional flow. In the small strain rate region, the Giesekus model predictions (solid

lines) can be brought into reasonable agreement with transient extensional data from the slip-spring model. However, deviations from the slip-spring simulation results can be observed for the larger strain rate region. In particular, the viscosity overshoot observed in the slip-spring simulations is not reproduced by the Giesekus model. Almost the same arguments are true for the PTT model predictions (dotted lines). Thus, the nonlinear shear and extensional slip-spring data are not simultaneously reproduced by the Giesekus and PTT models with a single nonlinear parameter.

Thus our attempt to fit slip-spring model predictions with those of common constitutive equations under both shear and extensional flows has not yet succeeded, although the Giesekus model can give good predictions under moderate shear flow. A complete constitutive equation might however be developed by replacing the nonlinear term of the Giesekus equation with a functional form sensitive to the flow type or by changing the nonlinear parameter α^G to a flow-type parameter that can distinguish shear from extensional flow. The latter idea would be tricky, and would require choosing a suitable metric of flow type that satisfies the proper invariance principles. If such a flow-type parameter is found that allows the model to predict results in both shear and extension, it would need to be checked by comparing its predictions to those of slip-spring simulations in mixed flows. These mixed flows are intermediate between shear and extension, for which the flow switches between shear to extension as a function of time. Such work is beyond the scope of this study, and therefore deferred to our future work.

D. The Effect of Entanglement Loss

Here, we examine the effect of the entanglement loss, which is one of the important nonlinear mechanisms and does not consider so far, on the rheological properties. We implement this effect by considering only a limiting case where the total number of slip-springs (Z_{total}) continually decreases and eventually becomes zero. Namely, when a slip-link goes through its chain end, this slip-link and the partner slip-link are simultaneously destroyed, and no regeneration of slip-links is considered. This method is similar to that employed by Moghadam and coworkers. From Figs. 9(a) and (b), the shear and extensional viscosities without the slip-spring regeneration are smaller than those with the slip-spring regeneration. This stress reduction corresponds to the decrease of the number of slip-springs seen in the insets of Figs. 9(a) and (b), and should contribute to shear or extension thinning behavior. As can be seen Fig. 9(a), the strain hardening is hardly observed for the case without the slip-spring regeneration. This is because the effect of slip-spring

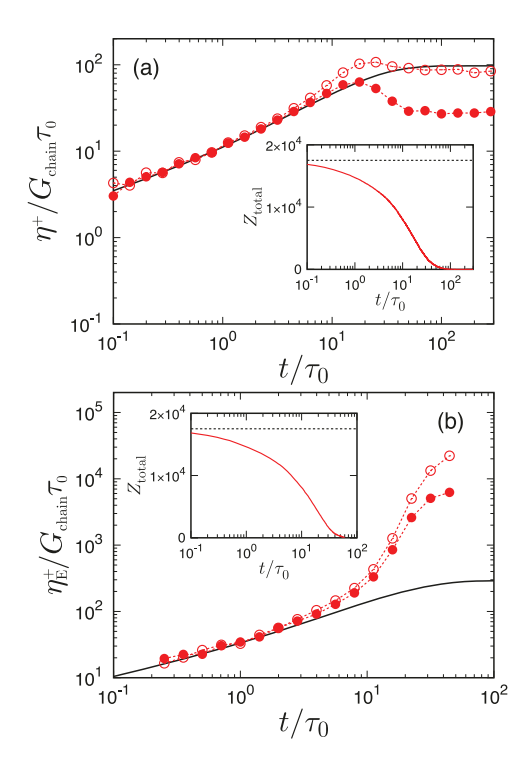


FIG. 9. (a) Shear and (b) extensional viscosities obtained by the micelle slip-spring model for $Z_{\text{tube}} = 5$ and $\zeta = 0.01$ with (open cirsles) and without (filled circles) the slip-spring regeneration. Strain rates are $\dot{\gamma}\tau_0 = 3*10^{-1}$ for the shear simulation, and $\dot{\varepsilon}\tau_0 = 1*10^{-1}$ for the extensional simulation. The linear viscosity growth functions are presented with the black solid lines. Dotted lines are added as guides to the eye. The insets are the total number of slip-springs in the system (Z_{total}). The horizontal dotted lines in the insets are the initial value of Z_{total} .

constraint is quickly lost due to the fast breakage. Nevertheless, the hardening behavior is expected to re-appear since the unentangled bead-spring model with the Fraenkel springs itself shows the hardening under fast shear, as shown in Fig. S9 in the supplementary material.

Since the extent of entanglement loss in nonlinear flow is still under investigation, our limiting cases of constant entanglement density and no regeneration of entanglements provide useful bounds on the expected behavior. A correct algorithm is somewhere between two cases since the entanglement regeneration process should exist even under flow. The correct entanglement regeneration algorithm should be developed first for polymers without breakage and rejoining events.

E. Comparison with Experimental Data

Finally, we present a comparison between the slip-spring results and experimental data for an aqueous solution of 100 mM cetylpyridinium chloride (CPyCl) with 45 mM sodium salicylate (NaSal) examined by Gaudino and coworkers. It should be noted that the experimental results for 100 mM CPyCl with 45 mM NaSal have a rather broad relaxation time distribution, as can be seen later in Fig. 10. However, it is typical that entangled linear WLM solutions with a sufficiently high surfactant or salt concentration show a Maxwell-type stress relaxation with a single relaxation time. This relaxation behavior is observed if the number of entanglements is large enough that the reptation dynamics is well separated from Rouse modes, and the breakage rate is fast enough that the relaxation process can be described by a single relaxation time. In this study, the computational cost limits the model to WLM solutions with moderate numbers of entanglements ($\lesssim 7$), which is not enough to show the Maxwell-type stress relaxation with a single relaxation time. Nevertheless, in the future, we hope to perform nonlinear simulations with a larger number of entanglements by developing a further computationally efficient code, or a constitutive model for well-entangled WLMs based on our micelle slip-spring model.

To test the ability of the slip-spring model to predict the nonlinear experimental data, the slip-spring parameters (i.e., the number of entanglements Z_{tube} and the dimensionless breakage time ζ) should be determined before performing linear and nonlinear rheological simulations. We can estimate Z_{tube} from the linear rheological data with the aid of the following relationship developed from the pointer algorithm by Tan and coworkers:³⁰

$$\frac{G_{\min}^{\in}}{G_{\min}^{\oplus}} = 0.317 \left) \frac{\langle L \rangle}{\ell_e} \sqrt{\frac{0.82}{\ell_e}} = 0.317 \langle Z_{\text{tube}} \rangle^{0.82}.$$
 (23)

Here, G_{\min}^{\Subset} is the local minimum in G^{\circlearrowleft} , G_{\min}^{\Subset} is the G^{\complement} value at the frequency at which G^{\image} shows its minimum value G_{\min}^{\Subset} , $\langle L \rangle_{i}$ is the average micelle length, and ℓ_{e} is the entanglement length. However, the target experimental data for the CPyCl/NaSal system does not have a clear minimum in G^{\circledR} (see Fig. 1(a) of Ref. 7). In this case, it is reasonable to assume that the $G_{\min}^{\complement}/G_{\min}^{\complement}$ value is a small number, $1 \simeq 2$, which gives $\langle Z_{\text{tube}} \rangle_{i} = 4 \simeq 9$. In this study, we therefore assume that the $G_{\min}^{\complement}/G_{\min}^{\complement}$ is 1.5, which gives $\langle Z_{\text{tube}} \rangle_{i} = 1.5$ is at about $\omega / 20 \text{ s}^{-1}$.) This $\langle Z_{\text{tube}} \rangle_{i} = 1.5$ is at about $\omega / 20 \text{ s}^{-1}$.) This $\langle Z_{\text{tube}} \rangle_{i} = 1.5$ is a lager than the value $\langle Z_{\text{tube}} \rangle_{i} = 2.5$ that Gaudino and coworkers obtained from an earlier scaling formula lacking a prefactor, namely $\langle Z_{\text{tube}} \rangle_{i} = 1.5$ with $\langle G_{\text{N}}^{0} \rangle_{i} = 1.5$ being a rough estimate of the plateau modulus since the experimental data does not show

a clear plateau from which to obtain $G_N^{0.7}$ Thus, the value of $Z_{tube} = 2.5$ is expected to be smaller than the more realistic value estimated from Eq. (23). For the dimensionless breakage time ζ , we use a relatively large value $\zeta = 10$ since the WLM solution is expected to be well outside of the fast breakage limit. This can be inferred from the fact that four modes are required to fit the LVE data (cf. Table I of Ref. 7).

In addition to Z_{tube} and ζ , we need to estimate the theoretical values of the stress $G_0^{(\text{theory})}$ and the unit time $\tau_0^{(\text{theory})}$ of the slip-spring model. Before computing these values, we estimate the plateau modulus of this WLM solution, G_N^0 . We use the following relation established by Tan and coworkers: 30 $G_{\rm N}^0/G_{\rm min}^{\in}=4.25/(G_{\rm min}^{\in}/G_{\rm min}^{\in})+0.625$. This equation is recommended for $G_{\min}^{\in}/G_{\min}^{\in}<10$, which is the case in our study. From our assumption of $G_{\min}^{\in}/G_{\min}^{\in}=1.5$ and $G_{\min}^{\in} = G^{\in}(\omega \prime 20 \text{ s}^{-1}) \prime 10 \text{ Pa}$, G_{N}^{0} is determined as $G_{N}^{0} \prime 35 \text{ Pa}$. Using the same procedure shown in our previous study, 36 we can determine $G_0^{(\mathrm{theory})}$ as $G_0^{(\mathrm{theory})} = G_\mathrm{N}^0/(0.8*~0.18)$ $\prime~~2*~10^2$ Pa. In the loosely entangled regime, G_N^0 is expressed as $G_N^0 = 9.75k_BT/\ell_{blob}^3$ where ℓ_{blob} is the blob size.²⁷ Using this equation and setting T = 300 K, we can compute ℓ_{blob} as 1.1×10^{-7} m. Taking for the persistence length ℓ_p the typical value $\ell_p = 25$ nm and using the relation $\ell_{blob} = \ell_e^{0.6} \ell_p^{0.4}$, we can determine the entanglement length ℓ_e as ℓ_e / 280 nm. Thus, the semi-flexibility factor α_e is $\alpha_e = \ell_e/\ell_p$ / 11, which is close to the standard value used in the slip-spring model, $\alpha_e^{ss} = 14$. In the slip-spring model, the unit of time τ_0 is $\tau_0 = \xi b^2/k_{\rm B}T = \xi b^3/k_{\rm B}T$ with $\xi^{\rm e}$ being the drag coefficient per unit micelle length. The value of ξ^{ϵ} can be computed using the drag coefficient for a cylinder of length ℓ_{blob} and micelle diameter d as $\xi \in 2\pi \eta_{\text{s}}/\ln(\ell_{\text{blob}}/d)$. Here, η_{s} is the solvent viscosity. From T = 300 K, $\eta_s = 0.85$ mPa ×s, and the typical value of d = 4 nm, the theoretical value of the unit time can be computed as $\tau_0^{\text{(theory)}}$ / 5 * 10 5 s.

Figure 10 compares the storage and loss moduli for the slip-spring simulation with $\ Z_{\text{tube}} = 7$ and $\ \zeta = 10$ (symbols) with the experimental data (lines). As noted in Sec. III A, we can use the slip-spring data for $t/\tau_0 \lesssim 3000$ to accurately evaluate G^{\in} and G^{\in} (cf. Fig. 2). Here, rather than plot the original G^{\in} and G^{\in} experimental data, we smooth these data using the fits to them by a set of Maxwell modes whose relaxation times and strengths are given in Table I of Ref. 7. The unit time and unit stress determined by shifting the dimensionless G^{\in} and G^{\in} curves to match the experimental G^{\in} and G^{\in} are $\tau_0 = 5*10^{-5}$ s and $G_0 = 2*10^2$ Pa, respectively. These values are the same as the theoretically determined unit time and stress since the semi-flexibility factor of the slip-spring model $\alpha_e^{ss} = 14$ is close to the experimental value of $\alpha_e / 11$. Unlike our previous study, 36 we need not correct τ_0 and G_0 to address the different α_e values between the slip-spring

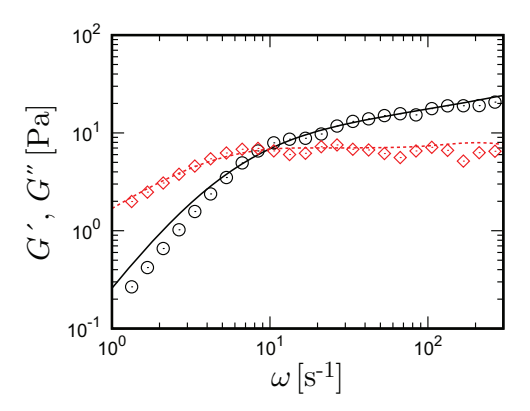


FIG. 10. Storage and loss moduli of slip-spring simulations with $Z_{\text{tube}} = 7$ and $\zeta = 10$ (symbols) compared to the experimental data (lines) for an aqueous solution of 100 mM CPyCl with 45 mM NaSal. The experimental data are reproduced by relaxation times and strengths shown in Table I of Ref. 7.

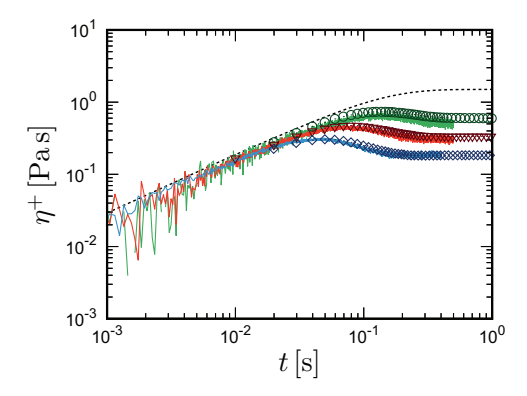


FIG. 11. Transient shear viscosity of slip-spring simulations (lines) compared to the experimental data (symbols) for aqueous solutions of 100 mM CPyCl with 45 mM NaSal. The linear viscosity growth function $\eta_0^+(t)$ obtained from the LVE data is plotted with the black dotted line. The strain rates are 20 s⁻¹ (green circles), 40 s⁻¹ (red reverse triangles), and 80 s⁻¹ (blue diamonds). The experimental data are taken from Fig. 2 of Ref. 7.

simulation and the experiment. From Fig. 10, we can see that G^{\in} and G^{\in} obtained from the slip-spring simulation are in reasonable agreement with the experimental data. This indicates that the choices of slip-spring parameters, i.e., Z_{tube} and ζ , are reasonable.

Figure 11 compares $\eta^+(t)$ predicted by the slip-spring simulations without SIMB and entanglement loss for $Z_{\text{tube}} = 7$ and $\zeta = 10$ (lines) with the experimental data (symbols). Here, we also use the values of τ_0 and G_0 determined in Fig. 10. The dimensionless shear rates $\dot{\gamma}\tau_0$ in the slip-spring model that correspond to the experimental values 20 s⁻¹, 40 s⁻¹, and 80 s⁻¹ are there-

fore about $\dot{\gamma}\tau_0$ / 1* 10 ³, 2* 10 ³, and 4* 10 ³, respectively. The slip-spring results in Fig. 11 are shown with solid lines, and $\eta_0^+(t)$ computed from the LVE data is presented with the black dotted line. Fig. 11 indicates that the slip-spring data are in good agreement with the experimental shear data. Again, this shows that the choices of slip-spring parameters are reasonable.

To the best of our knowledge, experimental data in extensional flow for WLM solutions with micelles of length accessible by the slip-spring model are not available currently. Extensional measurements for WLM solutions with low viscosities are typically conducted by the Capillary Breakup Extensional Rheometry (CaBER). However, the strain rate of the CaBER measurements is not constant over time, making it difficult to compare the extensional experimental data with the slip-spring data. Additionally, an initial step extensional strain in the CaBER measurements might affect the extensional viscosity. ¹⁴ It is difficult to produce the initial state of micellar chains for the slip-spring simulations. The comparison with extensional experiments is an important problem to study in the future.

IV. CONCLUSIONS AND SUGGESTIONS FOR FUTURE WORK

We have presented linear and nonlinear rheological predictions of a mesoscopic simulation model for entangled WLM solutions, the so-called "micelle-slip-spring model" based on the polymer slip-spring model proposed by Likhtman³⁷ with breakage and rejoining events added to reproduce WLM dynamics.³⁶ To capture the nonlinear rheological properties, instead of the Hookean springs employed in our previous study,³⁶ we introduced the Fraenkel potential for main-chain springs and slip-springs. Additionally, to improve extensional properties under strong extensional flow, we incorporated stress-induced micelle breakage into the micelle-slip-spring model. We used this extended model to examine both linear and nonlinear rheological properties.

In the linear response region, the relaxation modulus G(t) was computed using the Green-Kubo formula from the equilibrium simulation. We found that G(t) for Frankel springs differs slightly from that for Hookean springs due to the difference in spring potential. The results for G(t) are fitted using the multimode Maxwell model to determine relaxation times and strengths.

This micelle slip-spring model with Fraenkel springs can reproduce the characteristic rheological behavior in start-up and steady-state shear of WLM solutions. That is, the transient shear viscosities for moderate strain rates show the experimentally observed overshoot and the steady shear viscosities show the observed shear thinning. The experimentally observed hardening be-

havior under strong shear flow can be replroduced by the micelle slip-spring model with finite extensibility. The slip-spring simulation results for the strain rates where the chains do not show significant chain stretch were fitted by two common phenomenological constitutive equations: the Giesekus model and the PTT model. The steady shear viscosity obtained by the slip-spring model can be well reproduced by both constitutive models. Transient shear predictions by the Giesekus model are also in good agreement with those of the slip-spring model. This result is qualitatively the same as in experimental observations. In contrast, transient predictions by the PTT model (with the non-affine deformation parameter set to zero to avoid spurious oscillations in shear) deviate from those by the slip-spring model. These results indicate the Giesekus model captures better the shear properties of the slip-spring model for not so high shear rates than does the PTT model.

The micelle slip-spring model was also applied to predict rheological properties under uniaxial extensional flow. The Fraenkel potential prevents the overstretch of WLM chains under extensional flow, and thus we can reach steady state extensional viscosities. While the micelle slip-spring model reasonably reproduces the onset of extension thickening behavior, this model fails to predict extension thinning behavior observed in experiments. Thus, we incorporated stress-induced micelle breakage (SIMB) which allows the simulation results with SIMB to successfully capture extension thinning behavior. We also show the Giesekus and PTT constitutive model predictions with the same nonlinear parameter as under shear flow underestimate the slip-spring results. To reproduce the steady extensional data of the slip-spring model, a smaller value of the nonlinear parameter (corresponding to smaller deviations from the upper-convected Maxwell model) is needed to fit the slip-spring results in extensional flow. However, the constitutive model predictions even with the modified nonlinear parameter cannot capture the transient extensional viscosities especially under strong flow. Thus, it is not possible to predict both shear and extensional properties by the Giesekus and PTT models with a single constant nonlinear parameter.

Furthermore, we examined the effect of entanglement loss on rheological properties by considering the limiting case in which we disable the regeneration of slip-springs when previous ones disappear, so that the number of slip-springs continuously decreases and eventually becomes zero. We found that the stress without the slip-spring regeneration is smaller than that with the slip-spring regeneration. Thus, the effect of entanglement loss should contribute to shear/extension thinning behavior. A correct algorithm for entanglement loss is somewhere between two cases of constant entanglement density and no regeneration of slip-springs, and should be developed first for unbreakable polymers.

The slip-spring simulation results were also compared with experimental linear rheological and nonlinear shear data. The number of entanglements $\rangle Z_{\text{tube}}$ was estimated from the linear rheological data using the recent relation found by Tan and coworkers, 30 and the dimensionless breakage time ζ was set to be large based on the inference that the WLM solution is well outside of the fast breakage limit. The simulation results for G^{\in} and G^{\oplus} were compared with the experimental results, and the unit time τ_0 and the stress G_0 were determined. These τ_0 and G_0 are the same as expected theoretical values, indicating the validity of the chosen parameters. Moreover, nonlinear shear viscosities obtained by the slip-spring model are in reasonable agreement with the experimental shear data. These results support the predictive ability of the slip-spring model under homogeneous shear flow.

Further studies are required to understand more deeply the rheological properties of WLM solutions using the micelle slip-spring model. For example, strain hardening in nonlinear stress relaxation is experimentally detected in several WLM systems 63,64 which has been linked to shearinduced associations of WLMs. Hence, to reproduce strain hardening in nonlinear stress relaxation, it might be important to incorporate this mechanism into the micelle slip-spring model. Moreover, it would be interesting to examine the change in strain-rate dependence of shear stress, which is related to shear banding, caused by stress-induced acceleration of micelle breakage. Additionally, the extensional rheology obtained by the slip-spring model should be compared with experimental results. The current simulations are limited to homogeneous flow. To incorporate inhomogeneous shear such as shear banding, the equations of conservation of mass and momentum should be coupled. While "multiscale" slip-link simulations have been performed for unbreakable polymer melts, 65 such simulations are currently too extensive to be carried out for WLM solutions since an ensemble of many WLM chains is required. Thus, the fitting of predictions of the slipspring model by a phenomenological constitutive equation, which is attempted for the first time in this study, might be effective for such a purpose. This might be done more efficiently in the future with the aid of machine learning techniques.⁶⁶ We hope to continue our study along these directions.

SUPPLEMENTARY MATERIAL

See supplementary material for further results obtained from the slip-spring simulations.

ACKNOWLEDGMENTS

T.S. would like to express the gratitude to Prof. T. Taniguchi for his comments and fruitful discussion on this work. This work was partially supported by JSPS KAKENHI Grant Number 21K13893. R.G.L. was funded by the National Science Foundation under grant CBET-1907517. Any opinions, findings, and conclusions or recommendations expressed in this material are those of the authors and do not necessarily reflect the views of NSF.

REFERENCES

- ¹Larson, R. G., *The Structure and Rheology of Complex Fluids* (Oxford University Press, 1999).
- ²Shikata, T., H. Hirata, and T. Kotaka, "Micelle formation of detergent molecules in aqueous media: Viscoelastic properties of aqueous cetyltrimethylammonium bromide solutions," Langmuir **3**, 1081–1086 (1987).
- ³Berret, J. F., J. Appell, and G. Porte, "Linear rheology of entangled wormlike micelles," Langmuir **9**, 2851–2854 (1993).
- ⁴Soltero, J. F. A., J. E. Puig, and O. Manero, "Rheology of the cetyltrimethylammonium tosilatewater system. 2. Linear viscoelastic regime," Langmuir, **12**, 2654–2662 (1996).
- ⁵Shikata T., H. Hirata, E. Takatori, and K. Osaki, "Nonlinear viscoelastic behavior of aqueous detergent solutions," J. Non-Newtonian Fluid Mech. **28**, 171–182 (1988).
- ⁶Rehage, H., and H. Hoffmann, "Viscoelastic surfactant solutions: Model systems for rheological research," Mol. Phys. **74**, 933–973 (1991).
- ⁷Gaudino, D., S. Costanzo, G. Ianniruberto, N. Grizzuti, and R. Pasquino, "Linear wormlike micelles behave similarly to entangled linear polymers in fast shear flows," J. Rheol. **64**, 879–888 (2020).
- ⁸Yesilata B., C. Clasen, and G.H. McKinley, "Nonlinear shear and extensional flow dynamics of wormlike surfactant solutions," J. Non-Newtonian Fluid Mech. **133**, 73–90 (2006).
- ⁹Gurnon, A. K., and N. J. Wagner, "Large amplitude oscillatory shear (LAOS) measurements to obtain constitutive equation model parameters: Giesekus model of banding and nonbanding wormlike micelles," J. Rheol. **56**, 333–351 (2012).
- ¹⁰Helgeson, M. E., M. D. Reichert, Y. T. Hu, and N. J. Wagner, "Relating shear banding, structure, and phase behavior in wormlike micellar solutions," Soft Matter **5**, 3858–3869 (2009).

- ¹¹Helgeson, M. E., P. A. Vasquez, E. W. Kaler, and N. J. Wagner, "Rheology and spatially resolved structure of cetyltrimethylammonium bromide wormlike micelles through the shear banding transition," J. Rheol. **53**, 727–756 (2009).
- ¹²Inoue, T., Y. Inoue, and H. Watanabe, "Nonlinear rheology of CTAB/NaSal aqueous solutions: Finite extensibility of a network of wormlike micelles," Langmuir, **21**, 1201–1208 (2005).
- ¹³Rothstein, J. P., "Transient extensional rheology of wormlike micelle solutions," J. Rheol. **47**, 1227–1247 (2003).
- ¹⁴Bhardwaj, A., E. Miller, and J. P. Rothstein, "Filament stretching and capillary breakup extensional rheometry measurements of viscoelastic wormlike micelle solutions," J. Rheol. **51**, 693–719 (2007).
- ¹⁵Prud'homme, R. K., and G. G. Warr, "Elongational flow of solutions of rodlike micelles," Langmuir **10**, 3419–3426 (1994).
- ¹⁶Hu, Y., S. Q. Wang, and A. M. Jamieson, "Elongational flow behavior of cetyltrimethylammonium bromide/sodium salicylate surfactant solutions," J. Phys. Chem. **98**, 8555–8559 (1994).
- ¹⁷Walker, L. M., P. Moldenaers, and J. -F. Berret, "Macroscopic response of wormlike micelles to elongational flow," Langmuir **12**, 6309–6314 (1996).
- ¹⁸Shikata, T., S. J. Dahman, and D. S. Pearson, "Rheo-optical behavior of wormlike micelles," Langmuir **10**, 3470–3476 (1994).
- ¹⁹Schubert, B. A., E. W. Kaler, and N. J. Wagner, "The microstructure and rheology of mixed cationic/anionic wormlike micelles," Langmuir **19**, 4079–4089 (2003).
- ²⁰Oelschlaeger, C., M. Schopferer, F. Scheffold, and N. Willenbacher, "Linear-to-branched micelles transition: A rheometry and diffusing wave spectroscopy (DWS) study," Langmuir **25**, 716–723 (2009).
- ²¹Giesekus, H., "A simple constitutive equation for polymer fluids based on the concept of deformation-dependent tensorial mobility," J. Non-Newtonian Fluid Mech. **11**, 69–109 (1982).
- ²²Olmsted, P. D., "Perspectives on shear banding in complex fluids," Rheol. Acta **47**, 283–300 (2008).
- ²³Lerouge, S., and J. F. Berret, "Shear-induced transitions and instabilities in surfactant wormlike micelles," in *Polymer Characterization. Advances in Polymer Science*, edited by Dusek K. and Joanny J. F. (Springer, Berlin, Heidelberg, 2010) vol. **230**.
- ²⁴Rothstein, J. P., and H. Mohammadigoushki, "Complex flows of viscoelastic wormlike micelle solutions," J. Non-Newtonian Fluid Mech. **285**, 104382 (2020).

- ²⁵Cates, M. E., "Reptation of living polymers: Dynamics of entangled polymers in the presence of reversible chain-scission reactions," Macromolecules **20**, 2289–2296 (1987).
- ²⁶Turner, M. S., and M. E. Cates, "Linear viscoelasticity of wormlike micelles: A comparison of micellar reaction kinetics," J. Phys. II France **2**, 503–519 (1992).
- ²⁷Zou, W., and R. G. Larson, "A mesoscopic simulation method for predicting the rheology of semi-dilute wormlike micellar solutions," J. Rheol. **58**, 681–721 (2014).
- ²⁸Zou, W., X. Tang, M. Weaver, P. Koenig, and R. G. Larson, "Determination of characteristic lengths and times for wormlike micelle solutions from rheology using a mesoscopic simulation method," J. Rheol. **59**, 903–934 (2015).
- ²⁹Zou, W., G. Tan, H. Jiang, K. Vogtt, M. Weaver, P. Koenig, G. Beaucage, and R. G. Larson, "From well-entangled to partially-entangled wormlike micelles," Soft Matter **15**, 642–655 (2019).
- ³⁰Tan, G., W. Zou, M. Weaver, and R. G. Larson, "Determining threadlike micelle lengths from rheometry," J. Rheol. **65**, 59–71 (2021).
- ³¹Vasquez, P. A., G. H. McKinley, and L. P. Cook, "A network scission model for wormlike micellar solutions. I. Model formulation and viscometric flow predictions," J. Non-Newtonian Fluid Mech. 144, 122–139 (2007).
- ³²Pipe, C. J., N. J. Kim, P. A. Vasquez, L. P. Cook, and G. H. McKinley, "Wormlike micellar solutions: II. Comparison between experimental data and scission model predictions," J. Rheol. 54, 881–913 (2010).
- ³³Peterson, J. D., and M. E. Cates, "A full-chain tube-based constitutive model for living linear polymers," J. Rheol. **64**, 1465–1496 (2020).
- ³⁴Peterson, J. D., and L. G. Leal, "Predictions for flow-induced scission in well-entangled living polymers: The "living Rolie-Poly" model," J. Rheol. **65**, 959–982 (2021).
- ³⁵Peterson, J. D., and M. E. Cates, "Constitutive models for well-entangled living polymers beyond the fast-breaking limit," J. Rheol. **65**, 633–662 (2021).
- ³⁶Sato, T., S. Moghadam, G. Tan, and R. G. Larson, "A slip-spring simulation model for predicting linear and nonlinear rheology of entangled wormlike micellar solutions," J. Rheol. **64**, 1045–1061 (2020).
- ³⁷Likhtman, A. E., "Single-chain slip-link model of entangled polymers: Simultaneous description of neutron spin-echo, rheology, and diffusion," Macromolecules **38**, 6128–6139 (2005).

- ³⁸Masubuchi, Y., "Simulating the flow of entangled polymers," Annu. Rev. Chem. Biomol. Eng. **5**, 11–33 (2014).
- ³⁹Rubinstein, M., and R. H. Colby, *Polymer Physics* (Oxford University Press, 2003).
- ⁴⁰Uneyama, T., and Y. Masubuchi, "Multi-chain slip-spring model for entangled polymer dynamics," J. Chem. Phys. **137**, 154902 (2012).
- ⁴¹Zhu, J., A. E. Likhtman, and Z. Wang, "Arm retraction dynamics of entangled star polymers: A forward flux sampling method study," J. Chem. Phys. **147**, 044907 (2017).
- ⁴²Hu, Y. T., and A. Lips, "Kinetics and mechanism of shear banding in an entangled micellar solution," J. Rheol. **49**, 1001–1027 (2005).
- ⁴³Fraenkel, G. K., "Visco-elastic effect in solutions of simple particles," J. Chem. Phys. **20**, 642–647 (1952).
- ⁴⁴Ramírez, J., S. K. Sukumaran, and A. E. Likhtman, "Significance of cross correlations in the stress relaxation of polymer melts," J. Chem. Phys. **126**, 244904 (2007).
- ⁴⁵Doi M., and S. F. Edwards, *The Theory of Polymer Dynamics* (Oxford University Press, 1986).
- ⁴⁶Mandal, T., and R. G. Larson, "Stretch and breakage of wormlike micelles under uniaxial strain: A simulation study and comparison with experimental results," Langmuir **34**, 12600–12608 (2018).
- ⁴⁷Likhtman, A. E., and T. C. B. McLeish, "Quantitative theory for linear dynamics of linear entangled polymers," Macromolecules **35**, 6332–6343 (2002).
- ⁴⁸Ramírez, J., S. K. Sukumaran, and A. E. Likhtman, "Hierarchical modeling of entangled polymers," Macromol. Symp. **252**, 119–129 (2007).
- ⁴⁹Lin, Y. -H., Das A. K., "Monte Carlo simulations of stress relaxation of entanglement-free Fraenkel chains. I. Linear polymer viscoelasticity," J. Chem. Phys. **126**, 074902 (2007).
- ⁵⁰Ianniruberto, G., A. Brasiello, and G. Marrucci, "Modeling unentangled polystyrene melts in fast elongational flows," Macromolecules **52**, 4610–4616 (2019).
- ⁵¹Ianniruberto, G., and G. Marrucci, "Origin of shear thinning in unentangled polystyrene melts," Macromolecules **53**, 1338–1345 (2020).
- ⁵²Dalal, I. S., N. Hoda, and R. G. Larson, "Multiple regimes of deformation in shearing flow of isolated polymers," J. Rheol. **56**, 305–332 (2012).
- ⁵³Larson, R. G., *Constitutive Equations for Polymer Melts and Solutions* (Butterworth Swries in Chemical Engineering: Sydney, 1988).

- ⁵⁴Khan, S. A., and R. G. Larson, "Comparison of simple constitutive equations for polymer melts in shear and biaxial and uniaxial extensions," J. Rheol. **31**, 207–234 (1987).
- ⁵⁵Bird, R. B., R. C. Armstrong, and O. Hassager, *Dynamics of Polymeric Liquids* (John Wiley & Sons, 1987), Vol. 1 Fluid Mechanics.
- ⁵⁶Phan Thien, N., and R. I. Tanner, "A new constitutive equation derived from network theory," J. Non-Newtonian Fluid Mech. **2**, 353–365 (1977).
- ⁵⁷Syrakos, A., Y. Dimakopoulos, and J. Tsamopoulos, "Theoretical study of the flow in a fluid damper containing high viscosity silicone oil: Effects of shear-thinning and viscoelasticity," Phys. Fluids **30**, 030708 (2018).
- ⁵⁸Ramírez, J., S. K. Sukumaran, B. Vorselaars, and A. E. Likhtman, "Efficient on the fly calculation of time correlation functions in computer simulations," J. Chem. Phys. **133**, 154103 (2010).
- ⁵⁹Ferry, J. D., *Viscoelastic Properties of Polymers* (John Wiley & Sons, 1980).
- ⁶⁰Xu, J., Y. Tseng, and D Wirtz, "Strain hardening of actin filament networks: Regulation by the dynamic cross-linking protein α-actinin," J. Biol. Chem. **275**, 35886–35892 (2000).
- ⁶¹Lutz-Bueno, V., R. Pasquino, M. Liebi, J. Kohlbrecher, and P. Fischer, "Viscoelasticity enhancement of surfactant solutions depends on molecular conformation: Influence of surfactant head-group structure and its counterion," Langmuir **32**, 4239–4250 (2016).
- ⁶²Moghadam, S., I. Saha Dalal, and R. G. Larson, "Slip-spring and kink dynamics models for fast extensional flow of entangled polymeric fluids," Polymers **11**, 465 (2019).
- ⁶³Brown, E. F., W. R. Burghardt, and D. C. Venerus, "Tests of the Lodge-Meissner relation in anomalous nonlinear step strain of an entangled wormlike micelle solution," Langmuir **13**, 3902–3904 (1997).
- ⁶⁴Adams, A. A., M. J. Solomon, R. G. Larson, and X. Xia, "Concentration, salt and temperature dependence of strain hardening of step shear in CTAB/NaSal surfactant solutions," J. Rheol. 61, 967–977 (2017).
- ⁶⁵Sato, T., K. Harada, and T. Taniguchi, "Multiscale simulations of flows of a well-entangled polymer melt in a contraction-expansion channel," Macromolecules **52**, 547–567 (2019).
- ⁶⁶Seryo, N., T. Sato, J. J. Molina, and T. Taniguchi, "Learning the constitutive relation of polymeric flows with memory," Phys. Rev. Research **2**, 033107 (2020).